Journal of Materials Chemistry A

ROYAL SOCIETY OF CHEMISTRY

REVIEW

View Article Online
View Journal | View Issue

Cite this: J. Mater. Chem. A, 2023, 11, 8453

Recent progress in phosphide materials for thermoelectric conversion

Robert J. Quinn and Jan-Willem G. Bos *

Thermoelectric materials allow for the interconversion of heat and electricity. Rapid progress has been made in materials performance but there is a continuing need for the exploration of new materials and disruptive thermoelectric effects. Metal phosphides are currently gaining increasing attention as potential thermoelectric materials. Structural complexity often leads to low thermal conductivity despite the low atomic mass of P, which underpins promising thermoelectric figures of merit, zT. Despite the ability of phosphorus to form strong covalent bonds, including polyanion bonding, a key challenge remains to embed better electrical properties and large power factors. A highest $zT = 0.9$ has been observed in n-type Cd_3P_2, whilst promising performance under applied fields has been observed in topological materials, *e.g.* in the Dirac metal TaP. In this review, we summarise recent materials developments and analyse some of the underlying thermoelectric parameters of metal phosphide materials.

Received 3rd February 2023
Accepted 31st March 2023

DOI: 10.1039/d3ta00620d

rsc.li/materials-a

1. Introduction

Thermoelectric technology can be used in power generation, mW-scale ambient heat scavenging and in thermal management, where the benefits of durability and absence of moving parts outweigh high costs and modest efficiencies.[1,2] A good example is the radioisotope thermoelectric generators (TEGs) used by NASA to power satellites and rovers. There continues to be a need for improved thermoelectric materials, based on sustainable elements and processing, lowering costs, and increasing power outputs and cooling performance of devices.

For a single material, the thermoelectric performance is quantified by its figure of merit (zT):[3]

$$zT = \frac{S^2\sigma}{\kappa}T \quad (1)$$

Here S is the Seebeck coefficient, σ the electrical conductivity and κ the thermal conductivity, consisting of lattice κ_L and electronic κ_E components. Large zT is desirable, translating directly to higher device efficiency.[4]

Sustainability considerations and energy security have led to an enormous research effort to develop better thermoelectric materials.[5–9] This has been driven by new design concepts such as the phonon-glass electron-crystal, nanostructuring, electronic bandstructure engineering and by improved experimental characterisation of electrical and heat transport.[5–9] This has resulted in gradual increases in zT for a range of materials

Institute of Chemical Sciences and Centre for Energy Storage and Recovery, School of Engineering and Physical Sciences, Heriot-Watt University, Edinburgh, EH14 4AS, UK. E-mail: j.w.g.bos@hw.ac.uk

Dr Robert Quinn received his MChem degree in Chemistry from the University of Oxford (Exeter College) in 2017 and received his PhD from Heriot-Watt University in 2021 following study on Half-Heusler thermoelectric materials. He is currently a research associate on a Leverhulme Trust funded project, exploring metal phosphide phases as potential thermoelectric materials.

Dr Jan-Willem Bos is an Associate Professor in Energy Materials at Heriot-Watt University. His research interests are in the interplay between composition, structure, and functional properties of extended solids. A large part of his current research is focused on the design of thermoelectric materials, including half-Heusler alloys and the emerging metal phosphides that are the topic of this review.

with highest values approaching $zT = 3$ for SnSe,[10–13] greatly exceeding the traditional limit of $zT = 1$. The wide range of heat sources (temperatures) means there is a need for a range of thermoelectric materials. These also need to satisfy engineering requirements such as good electrical and thermal contacting, long term stability and mechanical strength, as well as matched thermal expansion for the n- and p-type legs that make up the basic thermoelectric couples in devices.[5–9] As yet, there is no leading thermoelectric n/p-type couple that would enable widespread cost-effective power generation or replace Bi_2Te_3 for ambient harvesting or cooling applications. For example, most of the very high zT materials considered for power generation, including Bi_2Te_3 itself,[14,15] PbTe[16–20] and GeTe[21,22] use tellurium, which is rare and hence expensive. SnSe has exceptional zT based on its ultralow κ and good electronic properties when doped,[23–25] but has limited high temperature stability.[26] Half-Heuslers boast large power factors ($S^2\sigma$) but their overall zT continues to be limited by large intrinsic thermal conductivity.[27,28]

There is considerable interest in Zintl thermoelectrics based on Sb, with antimonide skutterudites reported with large $S^2\sigma$ and zT[29–33] and more recently Mg_3Sb_2 phases with high zT near room temperature in n-type samples.[34–38] There are several excellent reviews and book chapters covering Sb-based thermoelectrics,[39–44] which support very good zT values, often substantially exceeding unity.

Metal phosphides have attracted limited attention as thermoelectrics but is a group of materials with high potential.[45] As will be shown, structural complexity often leads to intrinsically low lattice thermal conductivities, hence providing a platform for potentially large zT values. In fact, for many of the explored materials the challenge is to improve the electrical properties and increase $S^2\sigma$. From a chemical perspective, the wide range of accessible phosphorous anionic oxidation states allows for a range of structure types and chemical bonding. This includes P^0/P^- with a high degree of covalent bonding and polyanion formation, and the isolated P^{3-} anion which affords more familiar ionic structure types. In addition to its chemical versatility, phosphorus is highly abundant (11th most abundant element in the earth's crust)[46] and relatively low-cost. It also has a lower atomic mass (20 amu) than most other common anions in thermoelectric compounds, offering potential advantages in terms of gravimetric power output. Metal phosphide structures include analogues of well-known thermoelectric candidate materials (in particular of skutterudites, clathrates and tetrahedrites), but also comprise a range of unique structures, with semiconducting or semimetallic bandstructures which are of interest for thermoelectric exploration.

One reason for the limited historical interest in metal phosphide thermoelectrics is through association with white phosphorus.[46] This material consists of weakly linked P_4 molecules and is highly pyrophoric, reacting violently with oxygen to form P_2O_5 and further with water to form H_3PO_4. The formation of highly toxic PH_3 gas is also a concern in synthesis involving phosphorus.[46] However, red phosphorus, effectively consisting of $(P_4)_n$ oligomers, has much better stability and is commonly used for synthesis.[46] Once formed, metal phosphides can exhibit excellent stability,[47–50] in particular if more electropositive alkali and alkaline earth elements are avoided.

This review will start with an overview of the reported thermoelectric properties from the recent literature, and it will discuss some of the underlying electronic and thermal parameters. In subsequent sections a more detailed overview of the structures and properties of highlighted promising materials are given, including novel thermoelectric effects based on topological states. The review concludes with an outlook for the field. All structures shown in this review were drawn using the VESTA programme and are based on published crystallographic data.[51]

2. Evaluation of performance and underlying thermoelectric parameters

The electronic bandstructures of many known metal phosphide structures can be accessed *via* databases such as the Materials Project,[52] and the electronic properties have been the subject of a recent review.[45] From a chemical bonding (Zintl) perspective, it is anticipated that the valence band has a large anion (P) component with conduction band more heavily weighted towards the metal orbitals. Most metal-phosphides are experimentally found to be p-type, consistent with small cation deficiencies leaving a shortage of electrons to fill the anion derived conduction band, hence leaving holes, and causing p-type conduction. Notable exceptions are the high zT phase Cd_3P_2 and the topological material TaP.[53–56]

An overview of the reported thermoelectric parameters for a range of metal phosphides is given in Fig. 1. These include $S^2\sigma(T)$, $\kappa_L(T)$ and $zT(T)$, and the weighted mobility (μ_w), which was calculated from reported $S(T)$ and $\sigma(T)$ using an empirical model.[62] The power output of a thermoelectric generator is related to $S^2\sigma$, and as such it is an important engineering parameter. The materials reported so far have modest $S^2\sigma$, typically achieving values between 0.8 and 1.2 mW m^{-1} K^{-2} above 300 K (Fig. 1a). A notable exception is CaCuP with $S^2\sigma =$ 1.75 mW m^{-1} K^{-2}, possibly linked to its simple crystal structure.[50] Low values are found for $Zn_{0.75}Cu_2P_8$,[59,63] rich in P–P bonds and the clathrate $Ba_8Cu_{14}Ge_6P_{26}$,[57] which are both limited to $S^2\sigma < 0.4$–0.6 mW m^{-1} K^{-2}. In all cases, the reported $S^2\sigma$ are much smaller than state-of-the-art materials, that typically achieve power factors >4 mW m^{-1} K^{-2} and up to 10 mW m^{-1} K^{-2} for some low-defect half-Heusler phases.[27]

The weighted mobility μ_w gives the fundamental electronic performance of a material, independent of carrier doping, and is defined as follows:[62]

$$\mu_w = \mu_0 \left(m^*_{DoS}/m_e\right)^{3/2} \quad (2)$$

$$m^*_{DoS} = (N_v)^{2/3} m^*_b \quad (3)$$

$$N_v = \sum_i N_o N_b \quad (4)$$

Here μ_0 is the carrier mobility in the limit of Hall carrier concentration, $n_H \rightarrow 0$, m^*_{DoS} is the density of states effective

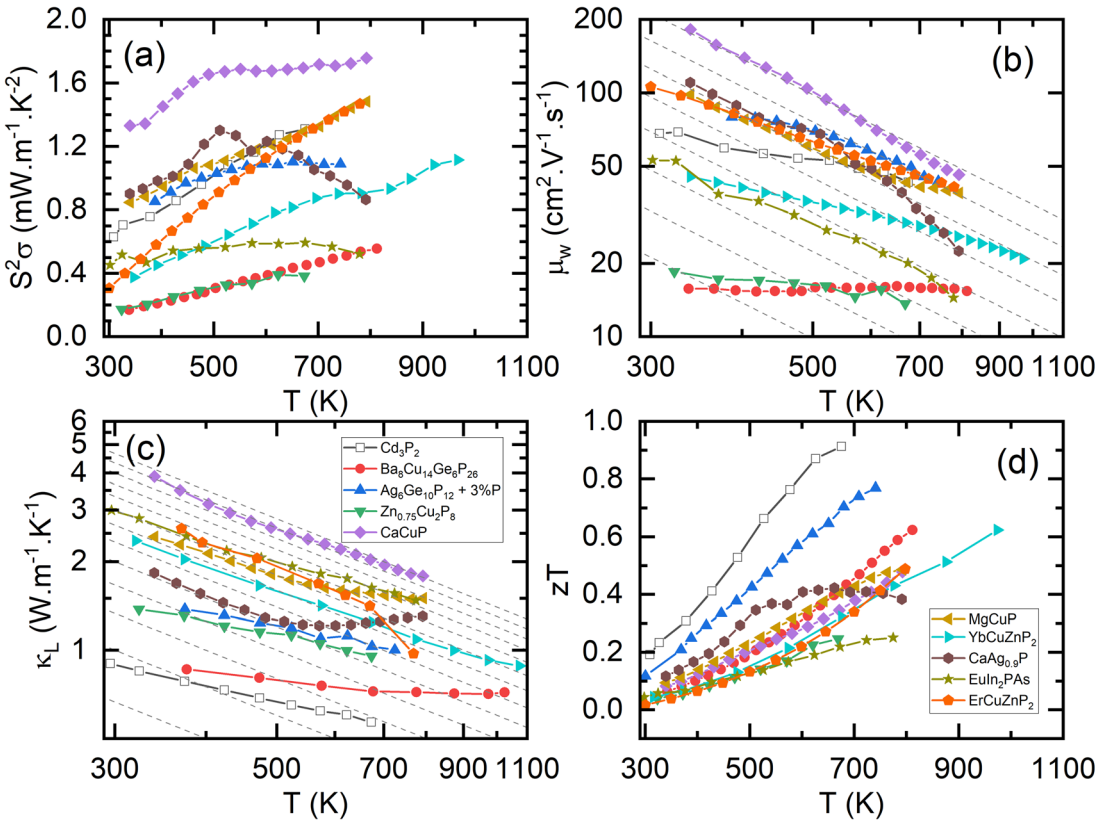

Fig. 1 Summary of the thermoelectric properties of promising metal phosphides. Panel (a) shows the power factor ($S^2\sigma$), (b) shows the weighted mobilities (μ_w); the dashed lines show a $T^{-1.5}$ acoustic phonon scattering dependence, (c) shows the lattice thermal conductivity (κ_L); the dashed lines show a T^{-1} Umklapp scattering dependence, and (d) shows the figure of merit (zT). Please note that panel (b) and (c) are plotted on a log–log scale (Cd_3P_2,[55] $Ba_8Cu_{14}Ge_6P_{26}$,[57] $Ag_6Ge_{10}P_{12}$,[58] $Zn_{0.75}Cu_2P_8$,[59] CaCuP,[50] MgCuP,[50] YbCuZnP$_2$,[47] CaAg$_{0.9}$P,[60] EuIn$_2$PAs,[61] ErCuZnP$_2$.[49]).

mass, which determines the magnitude of $S \propto m^*_{DoS}$, and m^*_b is the effective band mass of the charge carriers. N_v is the total valley degeneracy of the valence or conduction band extrema, which is the product of the degeneracy arising due to symmetry (N_o) and the degeneracy arising due to different bands (N_b). In the acoustic phonon scattering model μ_0 scales as $m^{*-2.5}_b$, meaning μ_w scales as$(N_v)^{2/3}m^{*-1}_b$.[64,65] As such thermoelectric materials should ideally have light charge carriers (low m^*_b), and a highly converged bandstructure near the Fermi energy (high N_v).[7]

Electronic bandstructure information available for metal phosphide phases is summarised in Table 1. Most compositions have band extrema at the Γ-point, which has the lowest possible $N_o = 1$. For example, n-type Cd_3P_2 has a single band at the Γ-point, with an exceptionally low $m^*_b \sim 0.09m_e$ leading to the highest Hall mobilities observed with $\mu_H \sim 1600$ cm^2 V^{-1} s^{-1} at room temperature.[55] The semimetallic p-type skutterudite CoP_3 is the only material in Table 1 that has similar low m^*_{DoS} and high mobilities (Table 1).[66] The low $m^*_{DoS}(N_v = 1)$ for Cd_3P_2 results in a relatively low S, yielding modest μ_w, similar to the A(CuZn)P_2 122-phases (Fig. 1b). The large zT observed for Cd_3P_2 is therefore mostly due to its low κ_L (Fig. 1c).

The best electronic performance so far is found for CaCuP, in part due to its second valence band ($N_b = 2$) at the Γ-point,[68] which affords a better trade-off between $S \propto m^*_{DoS}$ and mobility $\mu_0 \propto m^{*-1}_b$. Not all phosphide bandstructures are trivial. For example the tetrahedrite $Ag_6Ge_{10}P_{12}$ has a complex electronic structure, with multiple hole pockets in low symmetry positions, associated with lone pairs on Ge^{2+} cations.[67,69] Low dispersion (heavy) bands along the G–F and maxima located just outside the high symmetry Γ–H direction yield $m^*_{DoS} = 16.5m_e$ for $Ag_6Ge_{9.875}Ga_{0.125}P_{12}$.[67] The electronic quality of the $Ag_6Ge_{10}P_{12}$-based tetrahedrite phases is similar to Cd_3P_2 and the 122 phases (Fig. 1b).

An overview of the measured lattice thermal conductivities (κ_L) is given in Fig. 1c. Within the kinematic theory of heat transport, κ_L is given by:

$$\kappa_L = \frac{1}{3}C_v v_s \Lambda \left(v_s \sim \sqrt{\frac{k}{m}} \right) \quad (5)$$

Here, C_v is the heat capacity, v_s is the velocity of sound; related to the bond force constant (k) and average atomic mass (m); and Λ is the phonon mean free path. Materials with heavy atoms and weak bonds leading to low v_s, and strong anharmonicity leading to low Λ due to strong Umklapp scattering, are desired to achieve "intrinsically" low κ_L.[5,6,70] Phosphorus has a relatively low atomic mass and on that basis is not directly associated

Table 1 Overview of electronic parameters for selected metal phosphide thermoelectrics. Data includes conduction type (n/p), location and degeneracy of the valence/conduction band, density of states effective mass (m^*_{DoS}) derived using the single parabolic band model with acoustic phonon dominated scattering, reported Hall carrier concentrations (n_H) and mobilities (μ_H)

Composition	Type	Band	$m^*_{DoS}(m_e)$	n_H (cm^{-3})	μ_H ($cm^2\ V^{-1}\ s^{-1}$)
$Ag_6Ge_{10-x}Ga_xP_{12}$[67]	p	Multiple[a]	7.7–16.5	$1.1–11 \times 10^{20}$	1.11–1.84
CaCuP[50,68]	p	Γ ($N_v = 2$)	1.0	1.6×10^{20}	101
MgCuP[50,68]	p	Γ ($N_v = 1$)	1.7	2.4×10^{20}	29
$Cd_3P_{2-\delta}$[55]	n	Γ ($N_v = 1$)	0.09	$3.6–10.5 \times 10^{17}$	950–1690
$Cd_3P_{1-x}As_x$[53,54]	n	Γ ($N_v = 1$)	0.05–0.11	$6.1–28 \times 10^{17}$	850–9400
$ErCuZnP_2$[49]	p	Γ ($N_v = 2$ to 3)	0.88	2.7×10^{20}	53
$YbCuZnP_2$[47]	p	—	0.60	2.4×10^{20}	11.8
CoP_3[66]	p	Γ ($N_v = 1$)	0.11	3.26×10^{19}	748
$CeFe_4P_{12}$[66]	p	—	0.16	1.42×10^{19}	24.9
$CeRu_4P_{12}$[66]	p	—	2.26	1.8×10^{20}	6.0

[a] see Section 3.2 on tetrahedrites.

with low κ_L. Nevertheless, most compositions in Fig. 1c achieve $\kappa_L < 2$ W m^{-1} K^{-1} at elevated temperatures.

Using elastic properties from the Materials Project (Bulk and Shear moduli B and G),[52,75] initial approximations of κ_L for phosphide materials can be made. Longitudinal, transverse and average sound velocities (v_l, v_t and v_s), Debye temperatures (θ_D) and Grüneisen parameters (γ) were calculated[27] and are listed in Table 2.

A plot of experimental κ_L against the calculated v_s is given in Fig. 2. This shows a very clear correlation between calculated v_s and measured κ_L, as expected from eqn (5). The high-zT material Cd_3P_2 has $v_s \sim 2000$ m s^{-1} and has $\kappa_L < 1$ W m^{-1} K^{-1} at 300 K. The next lowest $\kappa_L < 2$ W m^{-1} K^{-1} materials are AgP_2 ($v_s \sim 2600$ m s^{-1}), Zn_3P_2 ($v_s \sim 3100$ m s^{-1}) and tetrahedrite $Ag_6Ge_{10}P_{12}$ ($v_s \sim 3000$ m s^{-1}), whilst CaCuP with its large μ_w has $v_s \sim 4000$ m s^{-1} and $\kappa_L \sim 4$ W m^{-1} K^{-1} at 300 K.

In general, a large v_s is caused by strong responses to compression and shear strain (large B and G, and hence strong bonds) and when material density is low. Inspection of Table 2 suggests that the trend in v_s (κ_L) is driven by the elastic moduli with changes in density having a smaller role. We note that these calculated values provide a general guide to the elastic properties but are far from exact and need confirmation from measurements.

Another important parameter is the bonding anharmonicity, quantified by the Grüneisen parameter (γ), which is a measure of the strength of phonon Umklapp scattering. For Cd_3P_2 the calculated γ from fitting the phonon bandstructure is 2.3–2.4, highlighting substantial anharmonic bonding, which combined with heavier mass of Cd results in the low observed κ_L.[55] Compared to CaCuP, with $\gamma \sim 1.35$ and its much higher v_s, the relatively large κ_L can be attributed to stronger bonds with reduced anharmonicity. A final point is that the phosphide skutterudites have by far the largest bulk moduli, coupled to low γ, leading to the highest v_s and κ_L values in Table 2.

Fig. 1d shows the figures of merit for leading phosphide materials. The highest reported $zT = 0.9$ at 673 K was reported for n-type Cd_3P_2 in 2022, linked to decent μ_w but largely driven by its low κ_L.[55] The best performance amongst the larger group of p-type materials is $zT \sim 0.7$ at 750 K for the tetrahedrite $Ag_6Ge_{10}P_{12}$, benefitting from several optimisation studies[58,69] since the original report in 2017.[48] Clathrates based on $Ba_8Cu_{16}P_{30}$ have been reported with $zT \sim 0.6$ at 800 K.[57,76] The

Table 2 Overview of gravimetric densities (ρ), bulk (B) and shear (G) moduli from the Materials Project, calculated longitudinal, transverse, and average sound velocities (v_l, v_t and v_s), Debye temperatures (θ_D), Grüneisen parameters (γ) and reported (experimental) lattice thermal conductivities (κ_L)

Composition	Materials project reference	ρ ($g\ cm^{-3}$)	B (GPa)	G (GPa)	v_l (m s^{-1})	v_t (m s^{-1})	v_s (m s^{-1})	θ_D (K)	γ	κ_L (W m^{-1} K^{-1})/ref.
CaCuP	mp-8432	4.01	74	51	5951	3566	3946	443	1.36	4.6[50]
CaAgP	mp-12277	4.89	61	43	4919	2965	3279	358	1.34	2.1[60]
MgCuP	mp-7352	4.41	94	48	5986	3299	3677	445	1.67	2.6[50]
SrCuP	mp-16321	4.81	66	46	5145	3092	3420	369	1.35	2.7[71]
Zn_3P_2	mp-2071	4.54	65	35	4959	2777	3090	345	1.61	1.3[72]
$CaZn_2P_2$	mp-9569	3.98	67	46	5678	3400	3762	417	1.37	3.3[73]
Cd_3P_2	Ref. [55]	5.60	64	18	3950	1760	1980	203	2.35	0.91[55]
$Ag_6Ge_{10}P_{12}$	mp-17862	5.09	65	36	4712	2659	2958	323	1.58	1.5[58]
CoP_3	mp-1944	4.38	149	115	8308	5124	5653	692	1.26	15.8[66]
$CeFe_4P_{12}$	mp-16272	5.17	161	132	8074	5053	5565	689	1.21	14.0[66]
$CeRu_4P_{12}$	mp-10069	5.74	167	110	7392	4378	4849	578	1.41	8.6[66]
AgP_2	mp-8200	4.86	62	26	4460	2313	2589	287	1.88	1.2[74]

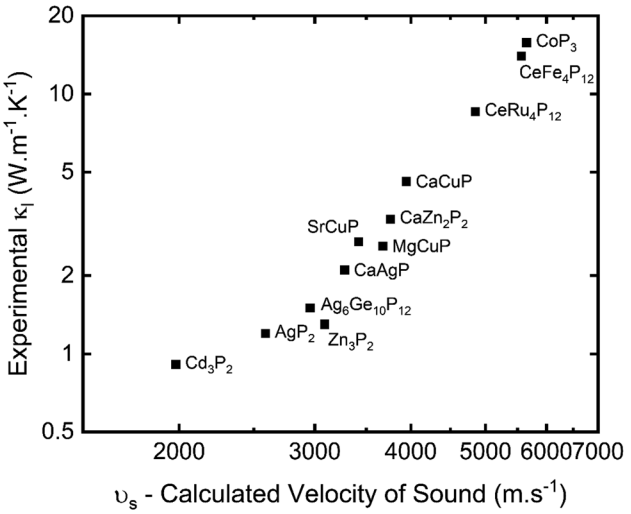

Fig. 2 Measured lattice thermal conductivity (κ_L) plotted against calculated velocity of sound (v_s) for selected metal phosphide thermoelectrics (see Table 2 for source data).

A(CuZn)P_2 122-phases reach $zT = 0.6$ at 800–1000 K,[47,49] whilst 111 phases, including CaCuP reach $zT = 0.5$ at 800 K.[50]

3. Phosphide thermoelectric materials

In this section, we will examine the leading phosphide materials in more detail, focusing on their crystal structure and bonding characteristics as well as thermoelectric performance. This will start with $ZnCu_2P_8$, a structure dominated by P–P bonding in Section 3.1. Section 3.2 will cover phosphide analogues of established phonon-glass electron-crystal systems (clathrate, skutterudite and tetrahedrite). Section 3.3 and 3.4 will focus on materials with 122 and 111 compositions, which do not exhibit P–P bonding. Section 3.5 will examine the n-type phases Cd_3P_2 and TaP, which display exceptional thermoelectric properties at high and low temperatures respectively.

3.1 $ZnCu_2P_8$ – a low-cost material with P–P bonding

$ZnCu_2P_8$, first reported in 2020,[15] is a good illustration of the range of bonding that phosphorus can exhibit. From an electron counting perspective, assuming Zn^{2+} and Cu^+ (both closed shell d^{10}), the P atoms must average to $[P_8]^{4-}$, requiring a large amount of P–P bonding.

The P–P network is quite complex (Fig. 3), although at its simplest, half the P atoms have three single P–P bonds and a single lone pair (*i.e.* P^0), and the other half have two P–P bonds with two lone pairs (*i.e.* P^-). Zn exists in a relatively uniform tetrahedral P coordination, while Cu has a more heavily deformed tetrahedral P environment. This neat separation of Zn and Cu sites may not be present in real samples however, with Cu^+/Zn^{2+} cation disorder being attributed to electronic and thermal transport features.[63]

Ab initio calculations show a strong dependence of the electronic structure and bandgap on Cu/Zn inversion.[63] This is reflected in the measured properties in the two studies on this material. $ZnCu_2P_8$ prepared using ball milling has an order of magnitude larger $\rho_{300\ K}$,[59] compared to high-temperature synthesis, which is found to have metal-like $\rho(T)$ and $S(T)$ above 100 K (but still with relatively high $\rho_{300\ K} \sim 50$ mΩ cm, $S_{300\ K} \sim 200$ μV K^{-1}),[63] suggesting a higher level of p-type doping, potentially linked to different Cu/Zn inversion or subtle deviations from nominal stoichiometry.[63] Overall, the performance of $ZnCu_2P_8$ is limited by a large $\rho(T)$ with highest observed $S^2\sigma = 0.11$ mW m^{-1} K^{-2} at 673 K.[59] In order to optimise the thermoelectric performance, the Cu^+/Zn^{2+} ratio was varied in the nominal $Zn_{1-x}Cu_{2+x}P_8$ ($-0.25 \leq x \leq 0.25$) series.[59] For $x < 0$ (increasing Zn – adding electrons), an increase in $\rho(T)$ was observed, yielding a highly resistive material. For $x > 0$ improvements to $S^2\sigma$ were found to be possible. To minimise CuP_2 impurities observed in the Cu-rich $Zn_{1-x}Cu_{2+x}P_8$ samples, $Zn_{0.75}Cu_2P_8$ was synthesised, yielding $S^2\sigma = 0.38$ mW m^{-1} K^{-2} at 673 K, and a highest reported $zT_{673\ K} = 0.25$. The most promising feature of $ZnCu_2P_8$ is its very low $\kappa = 1.05$–1.60 W m^{-1} K^{-1} at 300 K, decreasing to as low as ~0.8 W m^{-1} K^{-1} at 673 K. Despite the modest overall performance, $ZnCu_2P_8$ is a fascinating thermoelectric material with complex chemical bonding offering further possibilities for optimisation. It is based on abundant low-cost elements and has good stability under ambient conditions.[59,63]

3.2 Phosphide analogues of high-zT phonon-glass electron-crystal thermoelectrics: tetrahedrite, clathrate and skutterudite materials

The phonon-glass electron-crystal concept (PGEC) is one of the key guiding ideas of modern thermoelectrics research.[77] Its aim is to unite the low thermal transport of a structural glass with the good electrical properties of a crystalline material.

Key thermoelectric materials exhibiting PGEC behaviour are the skutterudites (*e.g.* $LaFe_3CoSb_{12}$)[78] and clathrates (*e.g.* $Ba_8Ga_{16}Ge_{30}$)[79] consisting of a conducting framework and rattling ions (La^{3+}/Ba^{2+} in the compositions above), causing glass-like κ_L, whilst the materials are crystalline. Tetrahedrites are chalcogenides (*e.g.* $Cu_{12}Sb_4S_{13}$)[80] with complex structures, characterised by extremely low κ_L linked to out-of-plane rattling vibrations of three-fold coordinated Cu ions.[81] There are phosphide analogues of all three of these important thermoelectric structure types, as illustrated in Fig. 4. These are discussed below in the following sections.

3.2.1. Tetrahedrite phosphides. The 'tetrahedrite' group spans a large number of minerals with the (simplified) general formula $A_6(B_4C_2)D_4Y_{12}Z$,[82] where A is Cu/Ag, B/C are late transition metals, D is a pnictide (cation) and Y/Z are S or Se. Tetrahedrite chalcogenides based on $Cu_{12}Sb_4S_{13}$ are promising thermoelectric materials, with reported zT values as high as 1.1, driven by very low $\kappa_L < 0.3$ W m^{-1} K^{-1}.[80,83–86]

$Ag_6Ge_{10}P_{12}$ can be written as $Ag_6(Ge_4Ge_2)Ge_4P_{12}Vac$ to match the tetrahedrite formula, where Vac is a vacancy in the structure. The presence of this vacancy is significant because it leads to the formation of an isolated $[Ag_6]^{4+}$ cluster.[87] Valence balancing to reach a semiconducting state requires a mixture of

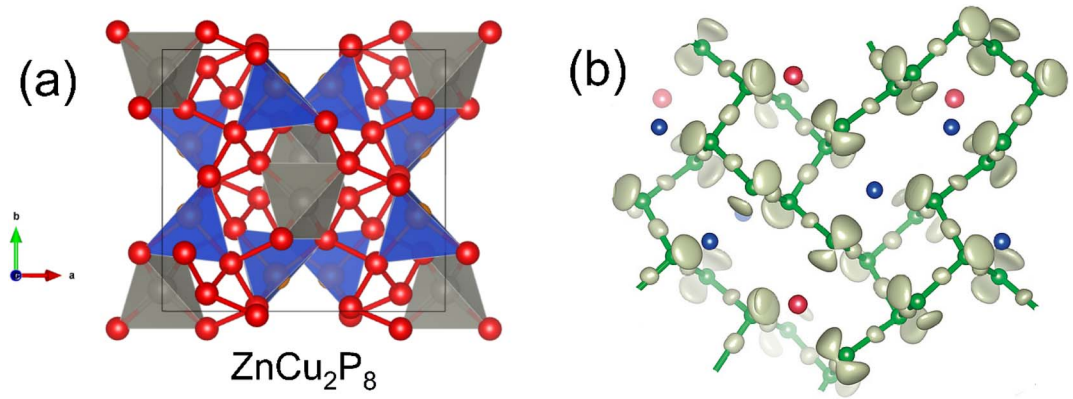

Fig. 3 Crystal structure of $ZnCu_2P_8$. Panel (a) shows the tetrahedral coordination of Zn (grey), Cu (blue) and the P–P network (red). Panel (b) shows the lone pair behavior of P (green), where P atoms with one lone pair coordinate to Cu (blue), and P atoms with 2 lone pairs bond to Zn (red). Panel (b) reproduced with permission from Nuss *et al.*, *Zeitschrift für Anorganische und Allgemeine Chemie*, 2020.[63]

oxidation states for Ge, leading to a formal assignment of $[Ag_6]^{4+}(Ge_4^{2+}Ge_2^{4+})Ge_4^{4+}P_{12}^{3-}$.[48]

$Ag_6Ge_{10}P_{12}$ is a p-type conductor, with semiconducting $\rho(T)$ and large $S_{300\ K} \sim 250\ \mu V\ K^{-1}$ (over 350 $\mu V\ K^{-1}$ in single crystals[48]).[48,58,88] Hole concentrations are sensitive to non-stoichiometry, controlled by nominal excess of P during synthesis. In one study 3% excess yielded the best electronic properties with largest $S^2\sigma \sim 1.1\ mW\ m^{-1}\ K^{-2}$ above 500 K.[58] Higher P excess leads to increased impurity phases, increased κ_L and degraded thermoelectric performance. Isovalent alloying with Cu and Sn in $Ag_{6-x}Cu_xGe_{10-y}Sn_yP_{12}$ has been found to lead to a reduction in κ_L, but the level of Cu substitution is limited

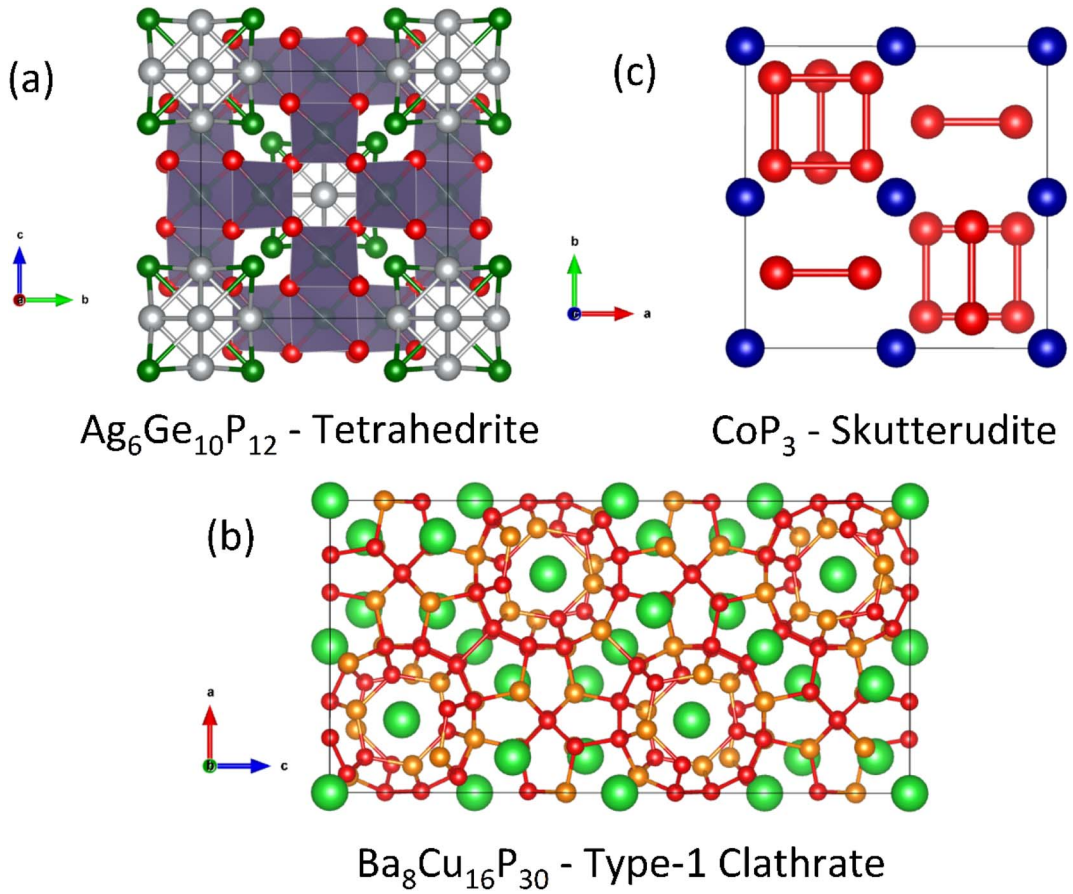

Fig. 4 Crystal structures of phosphide analogues of established phonon-glass electron-crystal thermoelectric materials. Panel (a) shows the $Ag_6Ge_{10}P_{12}$ tetrahedrite structure. Panel (b) shows the $Ba_8Cu_{16}P_{30}$ clathrate structure. Panel (c) shows the (unfilled) CoP_3 skutterudite structure with $[P_4]^{4-}$ squares (Ba = green, Co = blue, Cu = orange, Ag = grey, Ge = dark green, P = red).

due to deterioration of the electronic performance.[88] Hole doping using Ga in $Ag_6Ge_{10-x}Ga_xP_{12}$ is effective and can control the hole concentration, with some additional suppression of κ_L.[67]

The m^*_{DoS} is rather large for $Ag_6Ge_{10-x}Ga_xP_{12}$, between 8 and $16m_e$ depending on the Fermi level, due to the combination of a low dispersion band in the *G–F* direction and the contribution of a lower energy valence band in the *Γ–H* direction.[67] The complex band structure and measured m^*_{DoS} values are illustrated in Fig. 5.

As is the case for most phosphide materials, high performance in the tetrahedrites is derived from low thermal transport. In single crystal $Ag_6Ge_{10}P_{12}$, $\kappa_L \sim 1.75$ W m^{-1} K^{-1} is observed at 300 K, which is reduced to 1.3 W m^{-1} K^{-1} for polycrystalline samples, with lowest observed values ~0.8 W m^{-1} K^{-1} in $Ag_{5.7}Cu_{0.3}Ge_{10}P_{12}$.[48,67,88] One explanation for the low κ_L is the weak interaction between the covalent Ge–P framework and the enclosed $[Ag_6Ge_4]$ clusters, in which large thermal displacement parameters give Ag^+ a liquid-like behaviour.[48] Alternatively, the $[Ag_6]^{4+}$ cluster has been considered to act as a low energy "rattler", leading to suppression of acoustic phonon modes and low sound velocities.[58,69]

At present, the highest reported figures of merit are for $Ag_6Ge_{10}P_{12}$ + 3% P and the $Ag_6Ge_{10-x}Ga_xP_{12}$ series, which have $zT_{750\ K} \sim 0.7$.[58,69]

3.2.2. Clathrate phosphides. A small number of P-based clathrates have recently been reported in the literature,[89] and this is an area of growing interest. One of the leading thermoelectric compositions is the p-type type-I clathrate $Ba_8Cu_{14}Ge_6P_{26}$, which benefits from low $\kappa_{300\ K}$ ~0.85 W m^{-1} K^{-1} decreasing to 0.7 W m^{-1} K^{-1} at 1000 K.[57] In this material Ge is required to give the material a semiconducting electron count relative to the parent $Ba_8Cu_{16}P_{30}$ phase and also serves to suppress κ_L. $Ba_8Cu_{16}P_{30}$ has been reported to be metallic but with a large $S_{300\ K}$ ~50 μV K^{-1},[90] whilst off-stoichiometric $Ba_8Cu_{15.5}P_{30.5}$ is reported to be semiconducting.[91] This suggests that adjusting the Cu/P content is a possible route to control the thermoelectric properties. For $Ba_8Cu_{14}Ge_6P_{26}$, a high intrinsic $\rho(T)$ leads to a low $S^2\sigma$, which never exceeds 0.56 mW m^{-1} K^{-2}.[57] Fortunately, the low thermal conductivity leads to a good peak $zT_{812\ K} \sim 0.63$, which could be increased with further electronic optimisation. Similar $zT_{800\ K} = 0.62$ has been reported for $Ba_8Cu_{14}Zn_2P_{30}$,[76] where the Cu/Zn ratio can be used to optimise doping between metallic $Ba_8Cu_{16}P_{30}$ and a highly resistive $Ba_8Cu_{11.4}Zn_{5.6}P_{30}$ phase. Further work on clathrate phosphides would be of considerable interest due to their inherently low κ_L. Although probably not directly useful for thermoelectric applications, a gold phosphide clathrate, $Ba_8Au_{16}P_{30}$ has been reported to have extremely low κ_L, as low as 0.15 W m^{-1} K^{-1} at 400 K, attributed not only to the high atomic mass of Au, but also to

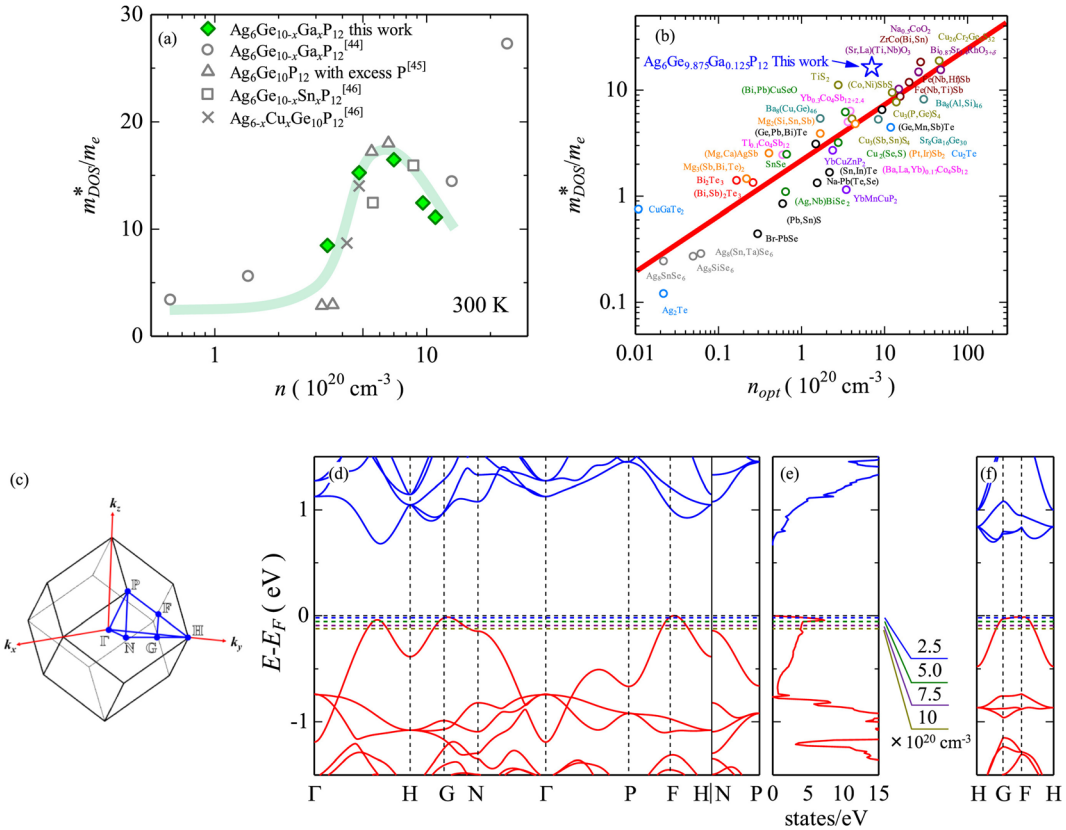

Fig. 5 Illustration of band convergence in $Ag_6Ge_{10-x}Ga_xP_{12}$. Panel (a) highlights the dependence of m^*_{DoS} on the hole concentration (Fermi energy). Panel (b) compares m^*_{DoS} against optimal doping for a range of thermoelectric systems. Panels (c–f) show the multiple bands that contribute to thermoelectric performance at different doping levels. Reproduced under a Creative Commons CC-BY license from Namiki *et al.*, *Materials Today Sustainability*, 2022.[67] References in Panel (a) correspond to the original manuscript.

twinning of crystallites on the nanoscale, leading to increased boundary scattering.[92] As prepared, this material is metallic and engineering the electron count of $Ba_8Au_{16}P_{30}$ to find a semiconducting state would be of interest. $BaNi_2P_4$, $BaCu_2P_4$ and $SrNi_2P_4$ form crystal structures which deviate from the familiar type-I clathrate.[93] Further work on $BaNi_2P_4$ found a stronger than predicted interaction between Ba and the covalent framework.[94] While these phases are quite metallic, they point to a large underexplored field still in its infancy when compared to Si and Ge based clathrate thermoelectrics with many more new compositions to be discovered.

3.2.3. Skutterudite phosphides. The A_xBX_3 skutterudite structure (named after $CoAs_3$) can be described in several ways. One viewpoint is a network of very strongly tilted corner-sharing BX_6 octahedra with up to 25% of void sites filled with rattler A ions. Another is a large primitive array of B (*e.g.* Co^{3+}) ions, inside of which 75% of sites are filled by $[X_4]^{4-}$ square rings with X–X bonding. The remaining 25% empty sites are available for filling with rattler ions to reduce κ_L. Antimonide skutterudites have attracted enormous interest and are prototypical PGEC materials, with high reported zT values approaching 2 after a sustained push to increase performance.[30,95] Phosphide skutterudites by contrast appear less promising, and not only because of their lower average atomic mass, large Bulk moduli and higher κ_L (Fig. 2 and Table 2).

Unfilled CoP_3 is an unusual material with a semiconducting $\rho(T)$ but with a magnitude typical of conductive metallic samples ($\sim$3 μΩ m between 5–1000 K), which is consistent with the low reported $S(T)$ of no more than 40 μV K^{-1}.[66,96] Early band structure calculations into CoX_3 skutterudite materials observed highly linear valence bands crossing a pseudo-band gap,[97,98] as illustrated for CoP_3 in Fig. 6. This unusual semimetallic bandstructure m_b^* may be the cause of poor thermoelectric performance in CoP_3.[30,31] The material is further held back by a large κ, although κ_L can be suppressed through the addition of La as "rattlers" in the vacant site,[96] with a reported reduction in κ_L from $\sim$15.8 W m^{-1} K^{-1} in CoP_3 to $\sim$3 W m^{-1} m^{-1} for $La_{0.24}CoP_3$.

More promising is p-type $CeFe_4P_{12}$, where Co has been replaced by Fe to balance the charge donation from the Ce^{4+} rattlers, maintaining a semiconducting electron count.[66,99] Interestingly, below 200 K $S(T)$ is slightly negative, with thermal excitations leading to p-type conduction at higher temperatures. The peak $S^2\sigma_{900\ K} = 0.7$ mW m^{-1} K^{-2} is substantially larger than for CoP_3, although κ remains large at all temperatures, limiting zT to $\sim$0.08 at 800 K.[99] $CeRu_4P_{12}$ similarly shows strong p-type semiconducting properties, with the decrease of $S(T)$ on heating pointing to a more significant bipolar character than the Fe analogue.[66] Analysis of room temperature Hall data using the SPB model assuming acoustic phonon scattering, reveals that the switch from Co(Fe) to Ru leads to a substantial increase in m_{DoS}^* from 0.11–0.16m_e to 2.26m_e as shown in Table 1.

3.3 The 1 : 2 : 2 phases – EZn_2P_2 and derivatives

A substantial number of EM_2P_2 compositions have been reported, with much interest generated on the back of the discovery of high-temperature superconductivity in the Fe pnictides. Generally compositions with M = Zn and Mn are found to be semiconducting. The two most common structure types are hexagonal $CaAl_2Si_2$ (illustrated in Fig. 7a) and tetragonal $ThCr_2Si_2$/$CeGa_2Al_2$ (shown in Fig. 7c).

In terms of thermoelectric performance, most work has focused on hexagonal p-type $CaZn_2P_2$ and $YbCuZnP_2$ derived

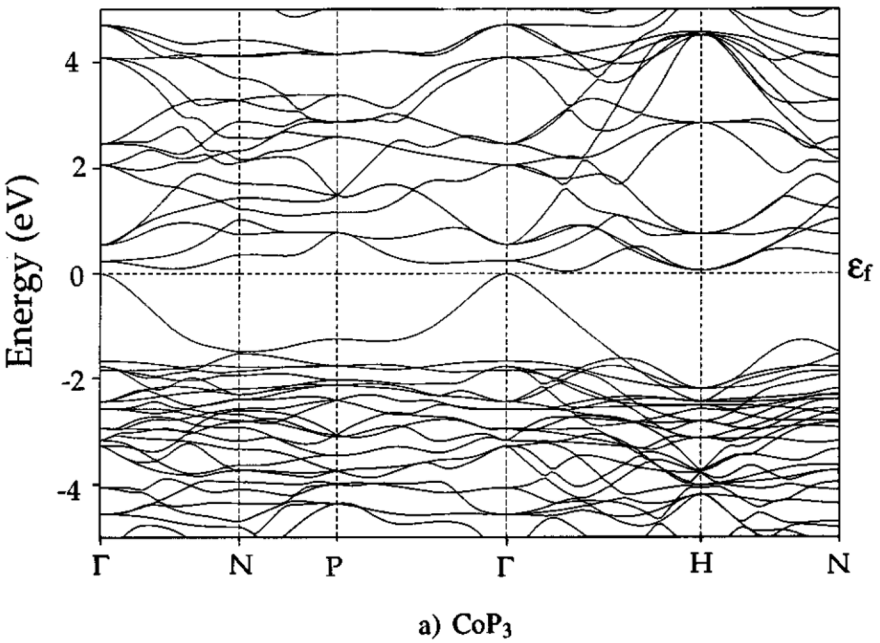

Fig. 6 Electronic band structure of skutterudite CoP_3. The material is largely gapped between −2 and 0 eV, but has one highly disperse quasi linear valence band at the Γ-point. Reproduced with permission from Llunell *et al.*, *Physical Review B*, 1996.[98]

compositions. In these materials the valence states can be simplified as $Ca^{2+}(Zn^{2+})_2(P^{3-})_2$ and $Yb^{3+}Cu^{+}Zn^{2+}(P^{3-})_2$.[47] The tetragonal $ThCr_2Si_2$ structure-type has more potential for intralayer P–P bonding, which would lead to a decrease in the oxidation state from P^{3-}. Observation of this structure with P–P bonding is limited to larger E cations, such as Ba.

As-synthesized $CaZn_2P_2$ has a high $\rho \sim 2$ Ω.m and $S \sim 300$ μV K^{-1} at 300 K, consistent with a large bandgap and little intrinsic doping,[47] with the Goldsmid-Sharp approximation suggesting $E_g \sim 0.6$ eV, although recent DFT calculations expect $E_g = 1.4$ eV.[100] Attempts to p-type dope *via* Cu substitution lead to a decrease in $\rho(T)$ at all temperatures, but $S(T)$ is also heavily suppressed at low temperatures, keeping $S^2\sigma < 0.02$ mW m^{-1} K^{-2}.[73] However, a sharp (and so far unexplained) increase in S above 600 K leads to a moderate $S^2\sigma_{970\ K} = 0.5$ mW m^{-1} K^{-2} in $CaZn_{1.9}Cu_{0.1}P_2$.[73] A similar temperature dependence has also been observed in Cu-doped Zn_3P_2, with sharp increases in S occurring above 600 K, coinciding with a discontinuity in $\sigma(T)$.[72] Mn^{2+} can be used instead of Zn^{2+} due to localisation of the $3d^5$ electrons, also yielding semiconducting materials with similar behaviour but a lower max zT,[73] but brings the prospect of coupling to magnetism.[101,102]

The performance of $YbCuZnP_2$-based compositions with 1 : 1 mixtures of Cu^{+} and Zn^{2+} (valence balanced through incorporation of Yb^{3+}) is much more promising. $YbCuZnP_2$ was found to have near constant $\rho(T) \sim 22$ μΩ m (5 orders of magnitude smaller than $CaZn_2P_2$) above 300 K and a high temperature $S \sim 160$ μV K^{-1} at 970 K, leading to $S^2\sigma_{970\ K} \sim 1.1$ mW m^{-1} K^{-2}. More recently the thermoelectric properties of other $RECuZnP_2$ materials (RE = Pr, Nd, Er) have been explored, in a study combining theory and experiment.[49] While not directly reported by the authors, $ErCuZnP_2$ displayed the largest $S^2\sigma$ of any reported phosphide material at that time, with $S^2\sigma_{780\ K} \sim 1.5$ mW m^{-1} K^{-2}.[49]

Also promising is the low κ_L for this structure type, consistently below 3 W m^{-1} K^{-1} at 300 K, approaching 1 W m^{-1} K^{-1} at 1000 K in the case of $CaZn_2P_2$ (Fig. 1). At present, $YbCuZnP_2$ has the largest reported $zT_{970\ K} \sim 0.63$ in this family of materials,[47] although at 800 K $ErCuZnP_2$ is reported with larger $zT = 0.5$.[49] Controlled doping (particularly in $CaZn_2P_2$) and employing isovalent alloying strategies may lead to further improvements.

There are a number of other interesting 1 : 2 : 2 compositions that do not have the $CaAl_2Si_2$ structure type. $LaMnCuP_2$ for example crystallises in the $BaCu_2S_2$-type structure (Fig. 7b), with the large La^{3+} cation stabilised by the an increased coordination number (CN) of 7 by phosphide ions.[103] This is supported by the existence of α-$BaZn_2P_2$ which also forms with the $BaCu_2S_2$-type structure.[104] Through higher temperature reaction conditions,

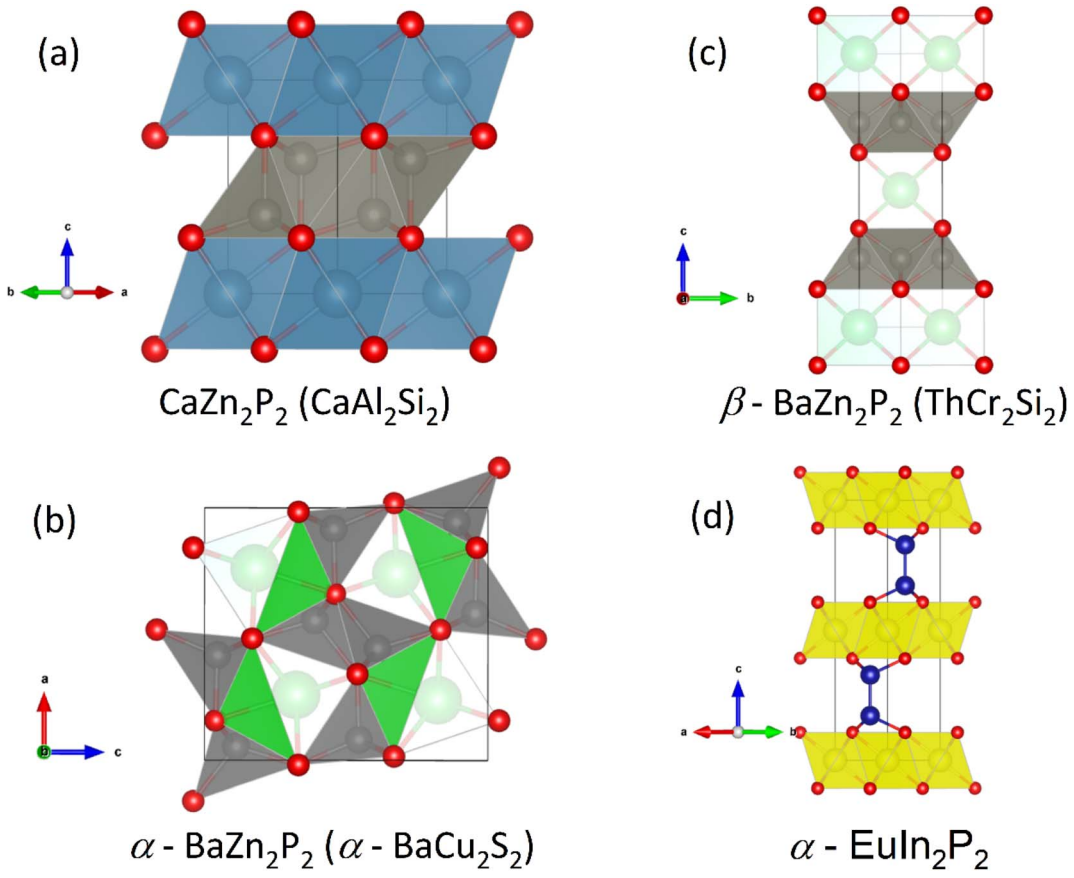

Fig. 7 Common crystal structures adopted by 1 : 2 : 2 phosphide thermoelectric materials. Panel (a) shows the $CaZn_2P_2$ structure ($CaAl_2Si_2$-type; Ca = cyan, Zn = grey, P = red), Panel (b) shows the α-$BaZn_2P_2$ structure (Ba = green), (c) Panel shows the β-$BaZn_2P_2$ ($ThCr_2Si_2$-type); structure and Panel (d) shows the α-$EuIn_2P_2$ structure (Eu = yellow, In = Blue).

β-$BaZn_2P_2$ was produced with the tetragonal $ThCr_2Si_2$-type structure which places Ba in a higher CN = 8 environment.[104] Initial thermoelectric property measurements of the α-phase confirm semiconducting $\rho(T)$ and $S_{300\ K} > 120\ \mu V\ K^{-1}$. With these observations in mind, there should be a large compositional and structural range for further investigation.

One final composition of note is $EuIn_2As_{2-x}P_x$, which differs from the above structures because it has direct In–In bonding (Fig. 7d).[61] Focussing on the P-rich compositions, the samples are degenerate semiconductors, with a largely temperature independent $S^2\sigma \sim 0.5$ mW m^{-1} K^{-2} between 300–800 K. Alloying leads to a substantial reduction in κ_L, consistent with mass and strain disorder, with a reduction from $\kappa_{L\ 300\ K} = 6.7$ W m^{-1} K^{-1} in $EuIn_2P_2$ to ~3 W m^{-1} K^{-1} in alloyed $EuIn_2PAs$. With this beneficial alloying contribution, $zT_{773\ K} \sim 0.25$ is achieved. Other isoelectronic $EuIn_2P_2$-type phosphides have been shown to exist experimentally,[105] which may also have promising thermoelectric properties.

3.4 The 1 : 1 : 1 phases – CaCuP, CaAgP and derivatives

A number of semiconducting phosphides with 1 : 1 : 1 composition have been reported. Assuming ionic P^{3-}, the electron donating metals are required to have formal +1 and +2 oxidation states. One larger group of materials satisfying this requirement is the Nowotny-Juza I-II-V phases, which are cubic semiconductors with a valence electron count of 8.[106] Their structures are closely related to the heavily investigated half-Heusler thermoelectrics,[27] differing only in preferred site occupancies.[106] An example of a phosphide Nowotny-Juza phase is LiZnP,[107] whose structure is shown in Fig. 8a. Here electronegative P occupies the pseudo-cubic site, whereas late transition metals such as Ni occupy this position in the 18 electron half-Heusler structure.[106] Unfortunately, exploration of these phases is difficult, with the alkali metal leading to instability in ambient conditions. A phosphide analogue of MgAgSb, with $zT \sim 1.4$ at temperatures below 550 K,[108,109] and good initial device properties,[110] would be of interest but has not been reported.

The remainder of this section will focus on the thermoelectric properties of the 111-compositions $CaAg_{0.9}P$, MgCuP, CaCuP and SrCuP.

The silver phosphide CaAgP has recently attracted interest as a possible nodal-line Direct semimetal,[111,112] although the presence of a predicted band-gap depended on the exchange correlation functional, with PBE-GGA giving a semimetallic bandstructure,[111,112] whereas a hybrid-functional gives a low band-gap semiconductor.[113] The CaAgP structure, originally discovered in 1979,[114] consists of edge-linked CaP_5 square based pyramids (Fig. 8b).

In our report, we observe large $S(T)$ values supporting a semiconducting bandstructure, with the metallic $\rho(T)$ likely arising due to Ag vacancies introducing holes into the material, with nominal CaAgP containing 3% Ag impurity and an Ag-site occupancy of ~0.9 from PXRD data.[60] $S^2\sigma(T)$ values in the

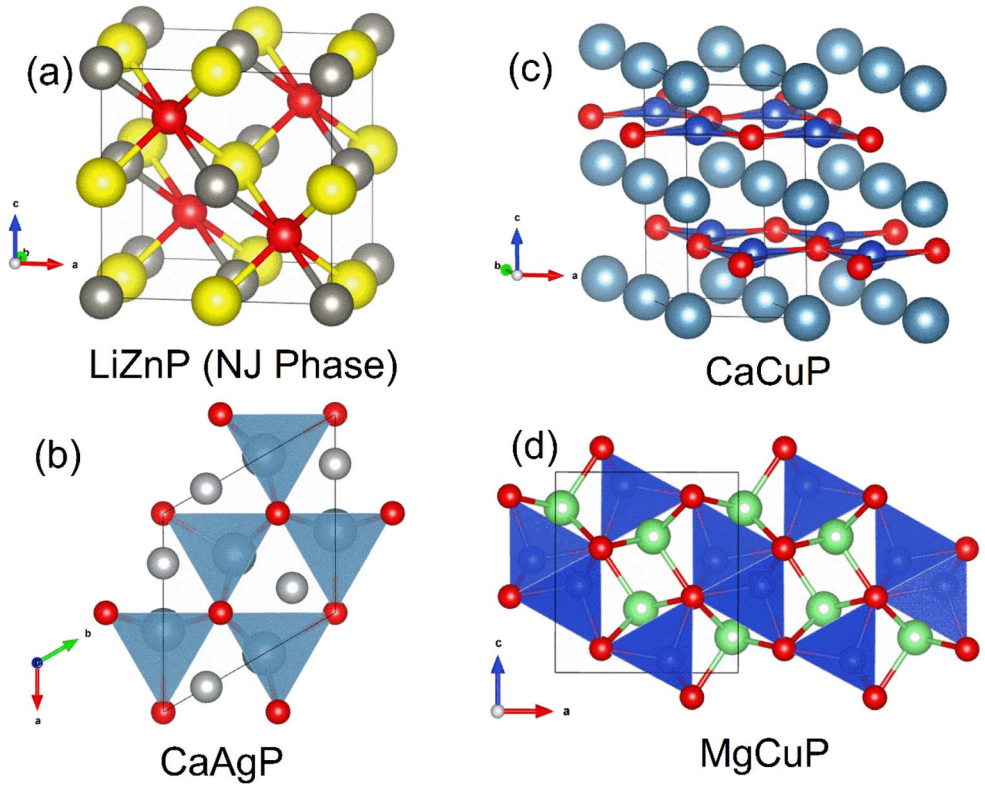

Fig. 8 Crystal structures of selected 1 : 1 : 1 metal phosphides. Panel (a) shows the cubic Nowotny-Juza phase LiZnP; Panel (b) shows CaAgP, consisting of CaP_5 and AgP_4 polyhedra; Panel (c) shows CaCuP with BN-like $[CuP]^{2-}$ layers spaced by Ca^{2+} cations; Panel (d) shows MgCuP with edge-linked CuP_4 tetrahedra in the b direction (P = red, Li = yellow, Zn = dark grey, Ca = cyan, Ag = light grey, Cu = blue and Mg = lime green).

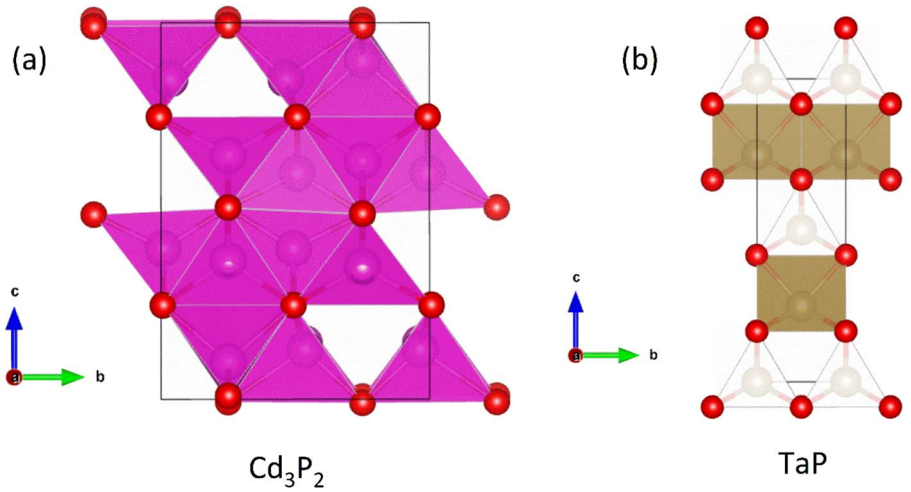

Fig. 9 Crystal structures of (a) Cd_3P_2 and (b) TaP (P = red, Cd = pink and Ta = brown). The Cd_3P_2 structure is tetragonal distortion of the cubic Ag_2O_3 structure. TaP consists of edge linked TaP_6 trigonal prisms, separated by corner-sharing TaP_4 tetrahedra.

targeted off-stoichiometric $CaAg_{0.9}P$ composition reach a peak of 1.25 mW m^{-1} K^{-2} at 550 K, decreasing at higher temperatures due to a bipolar decrease in $S(T)$. The thermal properties of $CaAg_{0.9}P$ are promising, with a low $\kappa_{L\ 340\ K} \sim 1.8$ W m^{-1} K^{-1} decreasing to a minimum of $\kappa_{L\ 600\ K} \sim 1.2$ W m^{-1} K^{-1}, although it appears that there is a significant bipolar contribution to κ at higher temperatures. Moderate electronic performance and low κ_L leads to a peak $zT_{600\ K} \sim 0.43$, which is promising for a largely unoptimized system. The thermoelectric properties of CaAgP have recently (the paper appeared during the proof stages of this review) been the subject of a computational study, confirming experimental findings.[115]

Following on from CaAgP, we reported the thermoelectric properties of MgCuP and CaCuP, based on sustainable elements and with low gravimetric densities.[50] These compositions each have different crystal structures (shown in Fig. 8c and d) and are different from CaAgP, again highlighting the structural diversity of the phosphides. CaCuP forms with hexagonal $[CuP]^{2-}$ layers isostructural with graphene or BN layers, separated by Ca^{2+} cations.[116] Where CaCuP can be viewed as pseudo-2D, the MgCuP structure consists of chains of edge-linked CuP_4 tetrahedra in the b-direction giving a pseudo-1D character to the structure (Fig. 8d).[117] Electronic bandstructure calculations for both phases exist in the literature, with calculated $E_g > 1$ eV for both phases.[68] An experimental follow-up, in the context of transparent semiconductors, found degenerate p-type behaviour arising due to Cu deficiency in CaCuP,[118] consistent with our observations.

Both CaCuP and MgCuP are p-type and have a very similar zT between 300–800 K, reaching ~0.5 at 790 K, although CaCuP has much better electronic properties while MgCuP has a lower κ_L.[50] At present CaCuP boasts the largest high temperature $S^2\sigma$ of any phosphide material reported in the literature, with a maximum $S^2\sigma_{790\ K} = 1.75$ mW m^{-1} K^{-2} (Fig. 1a) and an average value of 1.62 mW m^{-1} K^{-2} between 340–790 K, which is helpful for power generation. Unsurprisingly, CaCuP has one of the larger κ_L covered in this review, with $\kappa_{L\ 340\ K} \sim 3.9$ W m^{-1} K^{-1}, compared to 2.4 W m^{-1} K^{-1} for MgCuP, decreasing to 1.8 W m^{-1} K^{-1} and 1.5 W m^{-1} K^{-1} at 790 K respectively. From a thermoelectric perspective, CaCuP is the more promising of the two phases due to its better electronic performance and the absence of detrimental bipolar carrier effects at high temperatures.[50] A further complication with the MgCuP phase was found with increased amounts of Cu_3P and CuP_2 impurity phases observed upon heating, pointing to partial decomposition of the majority phases.[50] However, this effect appears to be reversible on cooling with observation of reversible hysteretic effects in the measured $S(T)$ and $\rho(T)$ on temperature cycling.

During review of this manuscript, Moll *et al.* reported on the thermoelectric properties of SrCuP,[71] which is isostructural to CaCuP. SrCuP was prepared using a mechanical alloying route and is more susceptible to oxidation than CaCuP with substantial $Sr_{10}(PO_4)_6O$ impurities and visible degradation of the SPS pellet in ambient conditions. In terms of its thermoelectric performance, SrCuP is a p-type degenerate semiconductor with peak $S^2\sigma_{700\ K} = 0.7$ mW m^{-1} K^{-2} and a minimum $\kappa_{L\ 600\ K} \sim 1.3$ W m^{-1} K^{-1}. The highest zT reported was $zT_{600\ K} = 0.2$, but improvements should be possible if better quality samples can be produced.

3.5 n-type compositions – Cd_3P_2 and topological magneto–thermoelectric TaP

A recent report on n-type Cd_3P_2 found the best thermoelectric performance for a phosphide material reported thus far, with $zT_{673\ K} \sim 0.91$.[55] Promising performance with $zT_{300\ K} = 0.2$ was originally reported as early as 1968 by Masumoto and Isomura,[53,54] where alloying with As was found to lead to $zT_{300\ K} \sim 0.33$, in large part due to suppression of κ_L. The crystal structure of Cd_3P_2 is a distortion of the cubic Ag_2O_3-type structure, with symmetry lowered from cubic to tetragonal. The structure consists of edge and vertex linked CdP_4 tetrahedra (Fig. 9a), while there are three distinct 6-coordinate environments for the P^{3-} anions.

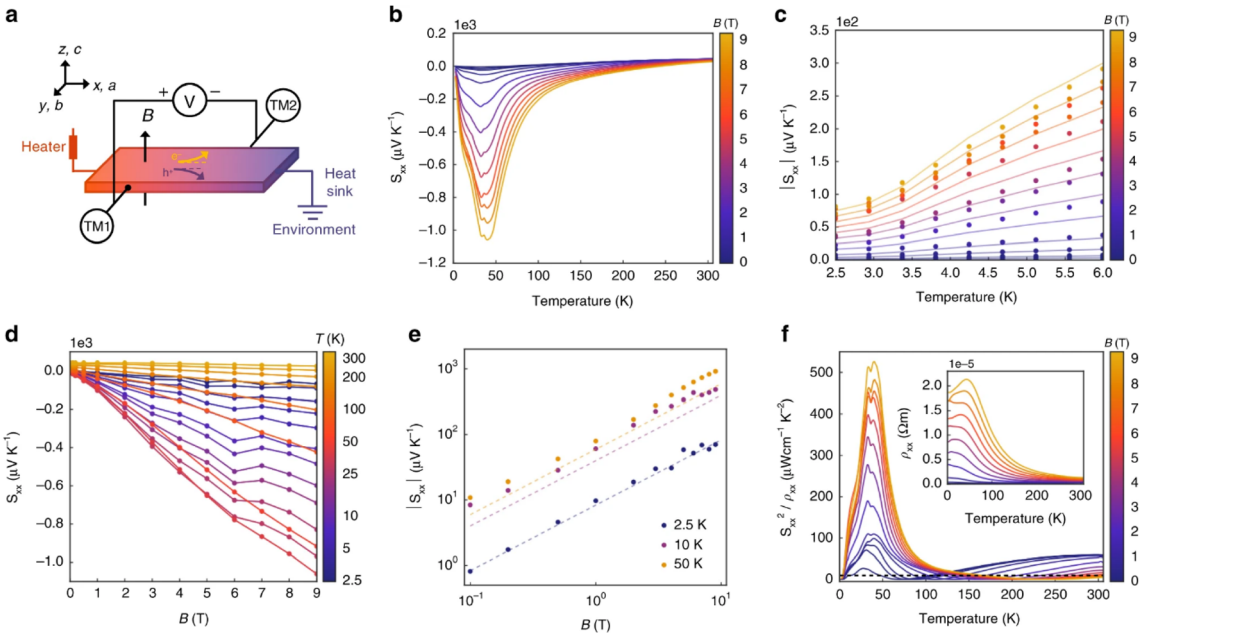

Fig. 10 Magneto–thermoelectric effect in TaP. Panel (a) illustrates the experimental setup used to measure the Seebeck coefficient in the x-direction (S_{xx}). Panel (b) shows the temperature dependence of S_{xx} at applied fields B_z between 2.5–300 K, and panel (c) highlights the 2.5–6 K region. Panel (d) shows the dependence of S_{xx} on the applied field at fixed temperatures, with panel (e) showing the same data on logarithmic axes. Finally, panel (f) shows the power factor in the x-direction as a function of temperature at fixed magnetic fields, showing the very large ${S_{xx}}^2/\rho_{xx} > 50$ mWm^{-1} K^{-2} near 45 K in 9T. Reproduced under a Creative Commons CC BY license from Han *et al.*, *Nature Communications*, 2020.[56]

At present, temperature dependent thermoelectric property data is only available from the 2022 study.[55] μ_H has been confirmed to be quite high from multiple sources,[53–55,119] with values ~1500 cm^2 V^{-1} s^{-1} at room temperature due to a low $m^*_{DoS} \sim 0.1m_e$, although μ_H can be lower when grain boundaries are present.[55] This low electron mass arises from a single highly dispersive conduction band minima at the Γ-point. Typical n_H values are on the order of 10^{17}–10^{18} cm^{-3} at 300 K,[53–55] which is on the lower end for thermoelectric materials. As expected from low extrinsic carrier doping, these materials have substantial intrinsic carrier effects, with a highly temperature dependent $n_H(T)$ and a strong bipolar decrease in $S(T)$ with increasing temperature.[55] The calculated band gap for the material is 0.46 eV. In the most highly doped sample, $S^2\sigma$ reaches large values for a system with such low m^*_{DoS}, with a maximum of 1.3 mW m^{-1} K^{-2} at 673 K.

As already discussed, the real driver behind the high zT is that $\kappa_L < 1$ W m^{-1} K^{-1} at all temperatures in the most recent report,[55] (or ~2 W m^{-1} K^{-1} in the original reports[53,54]). First principles calculations and acoustic measurements find low v_s are largely responsible for low κ_L.[55] In the phonon density of states, the acoustic phonon behaviour is dominated by the vibration of Cd atoms, while P atoms contribute more heavily to optical phonons.

Alloying in the $Cd_3P_{1-x}As_x$ solid solution was carried out in the 1970,[53,54] confirming the formation of a complete solid solution. Across the solid solution, all samples are n-type and degenerately doped. The alloying dependence of κ_L shows a decrease from either end member consistent with expected alloying behaviour, however an increase near $x = 0.5$ suggests partial ordering on the P/As site. The thermoelectric properties of single crystal Cd_3As_2 are interesting, showing strong magneto–thermoelectric effects attributed to linear dispersion in the conduction band.[120] The room temperature thermoelectric values for Cd_3P_2 with zero applied field are better however, so an examination of Cd_3P_2 in applied fields could prove to be interesting.

On the subject of magneto–thermoelectric effects, n-type TaP displays particularly interesting properties,[56] perhaps not in the context of power generation, but rather with the observation of the 'quantised thermoelectric Hall effect' (QTHE). In short, Weyl Semi-Metals (WSM) benefit from an energy independent density of states $g(E)$ which increases with applied magnetic fields, protected by the topological behaviour of the Weyl nodes. Since S is proportional to the logarithmic derivative of $g(E)$, the application of a magnetic field allows an applied field to induce large $S(B)$. In single crystal TaP, the QTHE has successfully been demonstrated, with $S_{xx}(9T) > 1000$ μV K^{-1} observed at ~45 K (Fig. 10b). As a semimetal, the applied field induced a substantial magnetoresistance in the sample, but at the maximum reported field of 9T, the power factor ${S_{xx}}^2\sigma$ exceeded 50 mW m^{-1} K^{-2} at ~45 K (Fig. 10f).[56] Such values are not ordinarily obtained for thermoelectric materials in thermodynamic equilibrium. The practicality of harvesting heat or applying the Peltier effect at 45 K under a 9T magnetic field is challenging and may prevent exploitation, however the results are exceptional.

4. Discussion

Metal phosphides are gaining increasing attention with a larger selection of materials now being investigated for their

thermoelectric performance. This has enabled more detailed insight into the underlying thermoelectric properties of metal phosphides. The current highest figures of merit are $zT_{673\ K} = 0.9$ for n-type Cd_3P_2 and $zT_{750\ K} = 0.7$ for p-type tetrahedrite $Ag_6Ge_{10}GaP_{12}$. In both cases, the performance is underpinned by low κ_L and relatively modest electronic properties (compared to the best performing thermoelectrics, such as Bi_2Te_3, SnSe, PbTe, GeTe, skutterudites and half-Heuslers).[5,7,9] Besides these two compositions, there are several other p-type compositions that reach $zT = 0.5$–0.6 at 700 K, including 111-type CaCuP and 122-type $YbCuZnP_2$. As observed for antimonide Zintl compositions, n-type conduction is relatively rare in metal phosphides. This is likely linked to the relative ease for metal deficiency in these compositions. One major conclusion is that despite the low atomic mass of P, low κ_L is commonly observed. This is linked to relatively "weak" chemical bonding (low k in eqn. (5)) in these materials, with a clear correlation between calculated ν_s and measured κ_L (Fig. 2). Searching for crystal structures with low bulk moduli (weak and anharmonic bonding) is therefore a promising route towards finding higher zT materials. Where calculations are not available, searching for crystal structures with mixtures of shorter and longer bonds as part of a single coordination environment might be a fruitful route.[24]

From the overview presented here, the main challenge is to improve the thermoelectric power factor in metal phosphides. Table 1 shows that investigated phosphides have m^*_{DoS} and μ_H values that are typical for semiconducting materials. The main issue appears to be that μ_0 (for a given m^*_{DoS}) lags behind that of thermoelectrics with large $S^2\sigma$,[62] hence compromising μ_w. Several materials have μ_w around 50–100 $cm^2\ V^{-1}\ s^{-1}$, with the clear outlier being CaCuP with 180 $cm^2\ V^{-1}\ s^{-1}$ which outperforms every other phosphide reported at all temperatures (Fig. 1b). However, even for CaCuP, the μ_w is only about 1/3 of high-power factor materials, such as the half-Heuslers[27,121–123] and antimonide skutterudites.[30–33] For CaCuP, the high μ_w is likely linked to its relatively simple crystal structure. The observation of large $\mu_w(T)$ for tetrahedrite $Ag_6Ge_{10}P_{12}$ is unexpected given its complex structure with unusual separation into weakly interacting $[Ag_6Ge_4]$ clusters within a $[Ge_6P_{12}]$ framework.[48] This suggests that the framework of vertex-sharing GeP_4 tetrahedra is effective in promoting hole transport. The low $\mu_w(T)$ for the two structures containing high degrees of P–P bonding ($Ba_8Cu_{14}Ge_6P_{26}$ and $Zn_{0.75}Cu_2P_8$), suggests that electrons in P–P bonds are localised and that this is not favourable for obtaining good electrical properties. There are several theoretical predictions of high thermoelectric performance, including in CuP_2,[124] and $BaAu_2P_4$.[125] These compositions or the features supporting good properties (bond hierarchy and low κ_L for $BaAu_2P_4$) are worthy of further investigation. Another interesting composition that was mentioned in the context of low κ_L is AgP_2 (Section 2). As prepared, this material is too insulating, but it could be of interest if it could be doped. Hall data reveal a low $m^*_{DoS} \sim 0.1m_e$ and $\mu_H = 50\ cm^2\ V^{-1}\ s^{-1}$.[74] Another potentially interesting silver phosphide is Ag_3SnP_7, which has a low $\kappa_L = 1.5\ W\ m^{-1}\ K^{-1}$ with no further thermoelectric characterisation.[126]

Assuming that electrical transport is dominated by acoustic phonon scattering (APS), the magnitude of μ_0 within the SPB model is related to the longitudinal velocity of sound, (ν_l), the band mass (m^*_b), the inertial carrier mass (m_I) and the deformation potential (E_{def}):[27]

$$\mu_0 = \frac{\pi e \hbar^4}{\sqrt{2}(k_B T)^{3/2}} \frac{{\nu_l}^2 d}{{E_{def}}^2} \frac{1}{m_b^{*3/2} m_I^*} \quad (6)$$

Here, E_{def} quantifies the coupling strength of the electrical transport to the crystal lattice (acoustic phonons). Collapsing the electrical transport of the materials in Table 1 onto one effective single band, assuming $m_1 = m^*_b$, and using the ν_l from Table 2 enables an estimate of E_{def}. For CaCuP and MgCuP $E_{def} = 13.4$ eV and 7.9 eV respectively. For Cd_3P_2 and $YbCuZnP_2$ values come out closer to 40 eV, although in both cases the temperature dependence of σ and μ_H don't match a typical degenerate semiconductor. At this point it is unclear if acoustic phonon scattering is indeed the dominant scattering mechanism, with optical phonon and ionised impurity scattering also likely to contribute, but the obtained values of E_{def} are fairly large for thermoelectric materials.[28,127–129] Further work on understanding electronic transport (carrier scattering) in these materials is needed and can provide avenues for further materials discovery and optimisation.

There are considerations for thermoelectric materials beyond zT, which limit application in popular thermoelectric systems. This includes finding matching n- and p-types, good mechanical properties, electrical and thermal contacting, stability under temperature cycling and during exposure to high temperatures.[5,9] Most of the phosphides discussed in this review are at least stable on the bench in ambient conditions, but it seems likely that some sort of encapsulation is needed for high-temperature operation.

A number of studies report thermogravimetric (TGA) and differential scanning calorimetry (DSC) data, generally under inert conditions (typical gas flow for TGA/sealed cups for DSC). For example, SrCuP is stable up to 1273 K from DSC,[71] but as discussed in Section 3.5, does readily oxidise in ambient conditions. By contrast MgCuP and CaCuP have good stability on the bench,[50] but a (reversible) decomposition occurs for MgCuP above 573 K. The $Ba_8Cu_{14}Ge_6P_{26}$ clathrate has good stability in inert conditions up to its melting point at 1100 K.[57] Investigation of $Ag_6Ge_{10}P_{12}$ in an open atmosphere showed decomposition above 750 K due to the evolution of P_4 gas.[48] By contrast, this composition is stable up to the melting point of 1000 K when heated inside a sealed quartz tube. Similarly Cd_3P_2 shows significant mass loss above 700 K in TGA. However, the sample can be consolidated using hot-pressing at 923 K.[55] $ZnCu_2P_8$ shows no thermal events during DSC measurements up to 960 K, above which mass loss is detected consistent with P_4 gas loss leaving behind the maximum oxidation state phases Cu_3P and Zn_3P_2.[63]

Materials design can be used to remedy stability issues as demonstrated for Cu_2Se, where Cu ion conduction can be suppressed, improving stability under operating conditions.[130] The high zT in Cd_3P_2 is an outstanding result showing that good performance is possible, but it won't be possible to use this composition due to the toxicity of Cd. Some of the 122 and 111 phase contain more abundant and benign constituent

elements. With further exploration of phosphide materials, electrical contacting, and measurement of mechanical and thermal properties will be essential to determining viability for device application.

5. Outlook

Metal phosphides have only very recently started to attract attention and are now approaching figures of merit, $zT = 1$ in both p- and n-type compositions. Whilst the overall performance lags behind those of state-of-the-art materials, this is a promising starting point for further exploration. Metal phosphides comprise a large class of materials with great structural and compositional (bonding) diversity afforded by the flexible oxidation state of P, from covalent P^0/P^{-1} to more ionic materials with P^{3-} anions. Hence, there is huge scope to discover better performing thermoelectrics.

The current best performing metal phosphides have low κ_L and are limited by relatively low μ_w. The low μ_w in the materials studied so far appears due to a relatively poor mobility (μ_0), when compared to thermoelectric materials with high $S^2\sigma$. When analysed within the APS limit, large E_{def} are found, suggesting a strong coupling with the lattice. Even if APS is not the dominant scattering mechanism, this result demonstrates that the carrier scattering is relatively high, compared to materials with comparable m^*_{DoS}. This leaves improving μ_w through m^*_{DoS}, and in particular by increasing N_v as increasing m^*_b degrades the mobility, as the most direct route to improve performance (eqn (2)–(4)). Investigation of high-zT tetrahedrite $Ag_6Ge_{10}P_{12}$ has found a highly converged band structure, whilst the large compositional range of 122- and 111-phases could afford opportunities for increasing N_v through solid-solution formation. It is also likely that materials with weaker APS (reduced electronic scattering) can be prepared. Targeted design of these materials would require a better understanding of the various carrier relaxation mechanisms. The observation of huge thermoelectric responses in the Weyl semimetal TaP, although driven by field induced increases in S, suggests that large power factors are possible in metal phosphides. Other now more routinely used optimisation strategies focused on defect-engineering,[6,8] including finding optimal dopants, control of intrinsic defects, nanostructuring, *etc*, have also not yet been widely applied to metal phosphides.

To conclude, metal phosphides remain a largely unexplored frontier area for thermoelectrics research, with many structures left to be discovered and explored. There is a clear need to improve understanding of the interplay between structure, bonding, and thermoelectric properties in metal phosphides, so that materials exploration can be accelerated. This should include using materials informatics and effective descriptors for high performance and first principles work focused on gaining microscopic understanding. There is no fundamental reason why higher zT values cannot be achieved. Given the established issues with high-temperature stability, this should focus on sub-ambient, room and moderate temperature applications.

Author contributions

Data analysis and visualisation (R. J. Q); manuscript writing – original draft (R. J. Q); conceptualisation, funding, project supervision, manuscript writing–review & editing (J. W. G. B.).

Conflicts of interest

The authors declare no competing financial interest.

Acknowledgements

The Leverhulme Trust is acknowledged for funding the research on metal phosphide thermoelectrics (RPG-2020-177).

References

1 D. M. Rowe, *CRC Handbook of Thermoelectrics*, CRC Press, 1995.
2 R. Funahashi, *Thermoelectric Energy Conversion*, Elsevier, 2021.
3 G. J. Snyder and E. S. Toberer, *Nat. Mater.*, 2008, **7**, 105–114.
4 G. J. Snyder and A. H. Snyder, *Energy Environ. Sci.*, 2017, **10**, 2280–2283.
5 Q. Yan and M. G. Kanatzidis, *Nat. Mater.*, 2022, **21**, 503–513.
6 Y. Zheng, T. J. Slade, L. Hu, X. Y. Tan, Y. Luo, Z. Z. Luo, J. Xu, Q. Yan and M. G. Kanatzidis, *Chem. Soc. Rev.*, 2021, **50**, 9022–9054.
7 T. Zhu, Y. Liu, C. Fu, J. P. Heremans, J. G. Snyder and X. Zhao, *Adv. Mater.*, 2017, **29**, 1605884.
8 X. Su, P. Wei, H. Li, W. Liu, Y. Yan, P. Li, C. Su, C. Xie, W. Zhao, P. Zhai, Q. Zhang, X. Tang and C. Uher, *Adv. Mater.*, 2017, **29**, 1602013.
9 X. L. Shi, J. Zou and Z.-G. Chen, *Chem. Rev.*, 2020, **120**, 7399–7515.
10 L. D. Zhao, G. Tan, S. Hao, J. He, Y. Pei, H. Chi, H. Wang, S. Gong, H. Xu, V. P. Dravid, C. Uher, G. J. Snyder, C. Wolverton and M. G. Kanatzidis, *Science*, 2016, **351**, 141–144.
11 C. Zhou, Y. K. Lee, Y. Yu, S. Byun, Z. Z. Luo, H. Lee, B. Ge, Y. L. Lee, X. Chen, J. Y. Lee, O. Cojocaru-Mirédin, H. Chang, J. Im, S. P. Cho, M. Wuttig, V. P. Dravid, M. G. Kanatzidis and I. Chung, *Nat. Mater.*, 2021, **20**, 1378–1384.
12 C. Chang, M. H. Wu, D. S. He, Y. L. Pei, C. F. Wu, X. F. Wu, H. L. Yu, F. Y. Zhu, K. D. Wang, Y. Chen, L. Huang, J. F. Li, J. Q. He and L. D. Zhao, *Science*, 2018, **360**, 778–782.
13 B. C. Qin, D. Y. Wang, X. X. Liu, Y. X. Qin, J. F. Dong, J. F. Luo, J. W. Li, W. Liu, G. J. Tan, X. F. Tang, J. F. Li, J. Q. He and L. D. Zhao, *Science*, 2021, **373**, 556.
14 S. I. Kim, K. H. Lee, H. A. Mun, H. S. Kim, S. W. Hwang, J. W. Roh, D. J. Yang, W. H. Shin, X. S. Li, Y. H. Lee, G. J. Snyder and S. W. Kim, *Science*, 2015, **348**, 109–114.
15 H. Y. Lv, H. J. Liu, J. Shi, X. F. Tang and C. Uher, *J. Mater. Chem. A*, 2013, **1**, 6831–6838.
16 Y. Wu, P. Nan, Z. Chen, Z. Zeng, R. Liu, H. Dong, L. Xie, Y. Xiao, Z. Chen, H. Gu, W. Li, Y. Chen, B. Ge and Y. Pei, *Adv. Sci.*, 2020, **7**, 1902628.

17 J. Zhang, D. Wu, D. He, D. Feng, M. Yin, X. Qin and J. He, *Adv. Mater.*, 2017, **29**, 1703148.
18 L. Fu, M. Yin, D. Wu, W. Li, D. Feng, L. Huang and J. He, *Energy Environ. Sci.*, 2017, **10**, 2030–2040.
19 G. Tan, F. Shi, S. Hao, L. D. Zhao, H. Chi, X. Zhang, C. Uher, C. Wolverton, V. P. Dravid and M. G. Kanatzidis, *Nat. Commun.*, 2016, **7**, 12167.
20 K. Biswas, J. Q. He, I. D. Blum, C. I. Wu, T. P. Hogan, D. N. Seidman, V. P. Dravid and M. G. Kanatzidis, *Nature*, 2012, **489**, 414–418.
21 A. Suwardi, J. Cao, L. Hu, F. Wei, J. Wu, Y. Zhao, S. H. Lim, L. Yang, X. Y. Tan, S. W. Chien, Y. Yin, W. X. Zhou, W. L. Mun Nancy, X. Wang, S. H. Lim, X. Ni, D. Li, Q. Yan, Y. Zheng, G. Zhang and J. Xu, *J. Mater. Chem. A*, 2020, **8**, 18880–18890.
22 X. Zhang, Z. Bu, S. Lin, Z. Chen, W. Li and Y. Pei, *Joule*, 2020, **4**, 986–1003.
23 L. D. Zhao, S. H. Lo, Y. S. Zhang, H. Sun, G. J. Tan, C. Uher, C. Wolverton, V. P. Dravid and M. G. Kanatzidis, *Nature*, 2014, **508**, 373.
24 S. R. Popuri, M. Pollet, R. Decourt, M. L. Viciu and J. W. G. Bos, *Appl. Phys. Lett.*, 2017, **110**, 253903.
25 I. Loa, S. R. Popuri, A. D. Fortes and J. W. G. Bos, *Phys. Rev. Mater.*, 2018, **2**, 085405.
26 S. R. Popuri, M. Pollet, R. Decourt, F. D. Morrison, N. S. Bennett and J. W. G. Bos, *J. Mater. Chem. C*, 2016, **4**, 1685–1691.
27 R. J. Quinn and J. W. G. Bos, *Mater. Adv.*, 2021, **2**(19), 6246–6266.
28 R. J. Quinn, G. B. G. Stenning and J. W. G. Bos, *J. Phys.: Energy*, 2022, **4**(2), 024005.
29 V. Shields, T. Caillat, J. P. Fleurial, A. Zoltan, L. Zoltan and M. Tuchscherer, *Twenty-first International Conference on Thermoelectronics, Proceedings ICT'02*, 2002, pp. 64–67.
30 G. Rogl, A. Grytsiv, P. Heinrich, E. Bauer, P. Kumar, N. Peranio, O. Eibl, J. Horky, M. Zehetbauer and P. Rogl, *Acta Mater.*, 2015, **91**, 227–238.
31 G. Rogl, A. Grytsiv, K. Yubuta, S. Puchegger, E. Bauer, C. Raju, R. C. Mallik and P. Rogl, *Acta Mater.*, 2015, **95**, 201–211.
32 G. Rogl and P. Rogl, *Curr. Opin. Green Sustainable Chem.*, 2017, **4**, 50–57.
33 G. Rogl, A. Grytsiv, F. Failamani, M. Hochenhofer, E. Bauer and P. Rogl, *J. Alloys Compd.*, 2017, **695**, 682–696.
34 H. Tamaki, H. K. Sato and T. Kanno, *Adv. Mater.*, 2016, **28**, 10182–10187.
35 J. Mao, J. Shuai, S. Song, Y. Wu, R. Dally, J. Zhou, Z. Liu, J. Sun, Q. Zhang, C. Dela Cruz, S. Wilson, Y. Pei, D. J. Singh, G. Chen, C. W. Chu and Z. Ren, *Proc. Natl. Acad. Sci. U. S. A.*, 2017, **114**, 10548–10553.
36 X. Shi, X. Wang, W. Li and Y. Pei, *Small Methods*, 2018, **2**, 1800022.
37 J. Zhang, L. Song, S. H. Pedersen, H. Yin, L. T. Hung and B. B. Iversen, *Nat. Commun.*, 2017, **8**, 13901.
38 J. Mao, H. Zhu, Z. Ding, Z. Liu, G. A. Gamage, G. Chen and Z. Ren, *Science*, 2019, **365**, 495–498.
39 S. M. Kauzlarich, S. R. Brown and G. J. Snyder, *Dalton Trans.*, 2007, (21), 2099–2107, DOI: **10.1039/B702266B**.
40 E. S. Toberer, A. F. May and G. J. Snyder, *Chem. Mater.*, 2010, **22**, 624–634.
41 S. M. Kauzlarich, A. Zevalkink, E. Toberer and G. J. Snyder, in *Thermoelectric Materials and Devices*, ed. I. Nandhakumar, N. M. White and S. Beeby, The Royal Society of Chemistry, 2016, DOI: **10.1039/9781782624042-00001**.
42 J. Shuai, J. Mao, S. Song, Q. Zhang, G. Chen and Z. Ren, *Mater. Today Phys.*, 2017, **1**, 74–95.
43 K. F. Liu and S. Q. Xia, *J. Solid State Chem.*, 2019, **270**, 252–264.
44 J. W. G. Bos, in *Inorganic Thermoelectric Materials: from Fundamental Concepts to Materials Design*, ed. A. V. Powell, The Royal Society of Chemistry, 2021, DOI: **10.1039/9781788019590-00216**.
45 J. H. Pöhls, A. Faghaninia, G. Petretto, U. Aydemir, F. Ricci, G. Li, M. Wood, S. Ohno, G. Hautier, G. J. Snyder, G. M. Rignanese, A. Jain and M. A. White, *J. Mater. Chem. C*, 2017, **5**, 12441–12456.
46 N. N. Greenwood and A. Earnshaw, *Chemistry of the Elements*, Butterworth-Heinemann, Oxford, 2nd edn, 1997.
47 V. Ponnambalam, S. Lindsey, W. Xie, D. Thompson, F. Drymiotis and T. M. Tritt, *J. Phys. D: Appl. Phys.*, 2011, **44**, 155406.
48 J. Nuss, U. Wedig, W. Xie, P. Yordanov, J. Bruin, R. Hübner, A. Weidenkaff and H. Takagi, *Chem. Mater.*, 2017, **29**, 6956–6965.
49 J. H. Pöhls, S. Chanakian, J. Park, A. M. Ganose, A. Dunn, N. Friesen, A. Bhattacharya, B. Hogan, S. Bux, A. Jain, A. Mar and A. Zevalkink, *Mater. Horiz.*, 2021, **8**, 209–215.
50 R. J. Quinn, C. Stevens, H. Leong, A. D. Huxley and J. W. G. Bos, *Chem. Commun.*, 2022, **58**, 11811–11814.
51 K. Momma and F. Izumi, *J. Appl. Crystallogr.*, 2011, **44**, 1272–1276.
52 A. Jain, S. P. Ong, G. Hautier, W. Chen, W. D. Richards, S. Dacek, S. Cholia, D. Gunter, D. Skinner, G. Ceder and K. A. Persson, *APL Mater.*, 2013, **1**, 011002.
53 K. Masumoto and S. Isomura, *J. Jpn. Inst. Met.*, 1968, **32**, 1116–1120.
54 K. Masumoto and S. Isomura, *Energy Convers.*, 1970, **10**, 129–133.
55 L. Fan, K. Peng, Z. Zhou, Y. Yan, C. Ran, H. Wang, G. Han, B. Zhang, X. Lu, G. Wang and X. Zhou, *Chem. Mater.*, 2022, **34**, 1620–1626.
56 F. Han, N. Andrejevic, T. Nguyen, V. Kozii, Q. T. Nguyen, T. Hogan, Z. Ding, R. Pablo-Pedro, S. Parjan, B. Skinner, A. Alatas, E. Alp, S. Chi, J. Fernandez-Baca, S. Huang, L. Fu and M. Li, *Nat. Commun.*, 2020, **11**, 6167.
57 J. Wang, O. I. Lebedev, K. Lee, J. A. Dolyniuk, P. Klavins, S. Bux and K. Kovnir, *Chem. Sci.*, 2017, **8**, 8030–8038.
58 A. Suwardi, L. Hu, X. Z. Wang, X. Y. Tan, D. V. M. Repaka, L. M. Wong, X. P. Ni, W. H. Liew, S. H. Lim, Q. Y. Yan, J. W. Xu, Y. Zheng and K. Hippalgaonkar, *ACS Appl. Mater. Interfaces*, 2020, **12**, 9150–9157.

59 J. Mark and T. Mori, *ACS Appl. Energy Mater.*, 2021, **4**, 4861–4866.
60 R. J. Quinn and J. W. G. Bos, *Appl. Phys. Lett.*, 2022, **120**, 073903.
61 K. Shinozaki, Y. Goto, K. Hoshi, R. Kiyama, N. Nakamura, A. Miura, C. Moriyoshi, Y. Kuroiwa, H. Usui and Y. Mizuguchi, *ACS Appl. Energy Mater.*, 2021, **4**, 5155–5164.
62 G. J. Snyder, A. H. Snyder, M. Wood, R. Gurunathan, B. H. Snyder and C. Niu, *Adv. Mater.*, 2020, **32**, 2001537.
63 J. Nuss, U. Wedig, K. Philippi and H. Takagi, *Z. Anorg. Allg. Chem.*, 2020, **646**, 1144–1150.
64 J. Bardeen and W. Shockley, *Phys. Rev.*, 1950, **80**, 72–80.
65 C. B. Vining, *J. Appl. Phys.*, 1991, **69**, 331–341.
66 A. Watcharapasorn, R. C. Demattei, R. S. Feigelson, T. Caillat, A. Borshchevsky, G. J. Snyder and J. P. Fleurial, *Jpn. J. Appl. Phys.*, 2000, **39**, 14.
67 H. Namiki, M. Kobayashi, K. Nagata, Y. Saito, N. Tachibana and Y. Ota, *Mater. Today Sustainability*, 2022, **18**, 100116.
68 B. A. D. Williamson, J. Buckeridge, J. Brown, S. Ansbro, R. G. Palgrave and D. O. Scanlon, *Chem. Mater.*, 2017, **29**, 2402–2413.
69 X. Shen, Y. Xia, G. Wang, F. Zhou, V. Ozolins, X. Lu, G. Wang and X. Zhou, *J. Mater. Chem. A*, 2018, **6**, 24877–24884.
70 T. Zhu, Y. Liu, C. Fu, J. P. Heremans, J. G. Snyder and X. Zhao, *Adv. Mater.*, 2017, **29**, 1605884.
71 A. Moll, A. Hamidou, J. C. Crivello, J. M. Joubert, E. Alleno and C. Barreteau, *J. Alloys Compd.*, 2023, **942**, 169123.
72 Y. Nagamoto, K. Hino, H. Yoshitake and T. Koyanagi, *Seventeenth International Conference on Thermoelectrics. Proceedings ICT98*, 1998, pp. 354–357, DOI: **10.1109/ICT.1998.740393**.
73 V. Ponnambalam and D. T. Morelli, *J. Electron. Mater.*, 2014, **43**, 1875–1880.
74 M. Miyata and M. Koyano, *Mater. Res. Express*, 2022, **9**, 055901.
75 M. De Jong, W. Chen, T. Angsten, A. Jain, R. Notestine, A. Gamst, M. Sluiter, C. K. Ande, S. Van Der Zwaag, J. J. Plata, C. Toher, S. Curtarolo, G. Ceder, K. A. Persson and M. Asta, *Sci. Data*, 2015, **2**, 1–13.
76 J. A. Dolyniuk, J. Wang, M. A. T. Marple, S. Sen, Y. Cheng, A. J. Ramirez-Cuesta and K. Kovnir, *Chem. Mater.*, 2018, **30**, 3419–3428.
77 G. A. Slack, in *CRC Handbook of Thermoelectrics*, ed. D. M. Rowe, CRC Press, Boca Raton, FL, 1995, p. 407.
78 B. C. Sales, D. Mandrus and R. K. Williams, *Science*, 1996, **272**, 1325–1328.
79 M. Christensen, S. Johnsen and B. B. Iversen, *Dalton Trans.*, 2010, **39**, 978–992.
80 X. Lu, D. T. Morelli, Y. Xia, F. Zhou, V. Ozolins, H. Chi, X. Zhou and C. Uher, *Adv. Energy Mater.*, 2013, **3**, 342–348.
81 S. O. Long, A. V. Powell, S. Hull, F. Orlandi, C. C. Tang, A. R. Supka, M. Fornari and P. Vaqueiro, *Adv. Funct. Mater.*, 2020, **30**, 1909409.
82 C. Biagioni, L. L. George, N. J. Cook, E. Makovicky, Y. Moëlo, M. Pasero, J. Sejkora, C. J. Stanley, M. D. Welch and F. Bosi, *Am. Mineral.*, 2020, **105**, 109–122.
83 J. Heo, G. Laurita, S. Muir, M. A. Subramanian and D. A. Keszler, *Chem. Mater.*, 2014, **26**, 2047–2051.
84 J. Wang, M. Gu, Y. Bao, X. Li and L. Chen, *J. Electron. Mater.*, 2016, **45**, 2274–2277.
85 H. Hu, H. L. Zhuang, Y. Jiang, J. Shi, J. W. Li, B. Cai, Z. Han, J. Pei, B. Su, Z. H. Ge, B. P. Zhang and J. F. Li, *Adv. Mater.*, 2021, **33**, 2103633.
86 P. Vaqueiro, G. Guélou, A. Kaltzoglou, R. I. Smith, T. Barbier, E. Guilmeau and A. V. Powell, *Chem. Mater.*, 2017, **29**, 4080–4090.
87 H. G. von Schnering and K. G. Hausler, *Rev. Chim. Miner.*, 1976, **13**, 71–81.
88 H. Namiki and Y. Ota, *Jpn. J. Appl. Phys.*, 2020, **59**, 075508.
89 J. Wang, J. A. Dolyniuk and K. Kovnir, *Acc. Chem. Res.*, 2018, **51**, 31–39.
90 D. Huo, T. Sasakawa, Y. Muro and T. Takabatake, *Appl. Phys. Lett.*, 2003, **82**, 2640–2642.
91 J. Dünner and A. Mewis, *Z. Anorg. Allg. Chem.*, 1995, **621**, 191–196.
92 J. Fulmer, O. I. Lebedev, V. V. Roddatis, D. C. Kaseman, S. Sen, J. A. Dolyniuk, K. Lee, A. V. Olenev and K. Kovnir, *J. Am. Chem. Soc.*, 2013, **135**, 12313–12323.
93 J. A. Dolyniuk, J. Wang, K. Lee and K. Kovnir, *Chem. Mater.*, 2015, **27**, 4476–4484.
94 J. Wang, J. A. Dolyniuk, E. H. Krenkel, J. L. Niedziela, M. A. Tanatar, E. I. Timmons, T. Lanigan-Atkins, H. Zhou, Y. Cheng, A. J. Ramirez-Cuesta, D. L. Schlagel, U. S. Kaluarachchi, L. L. Wang, S. L. Bud'ko, P. C. Canfield, R. Prozorov, O. Delaire and K. Kovnir, *Chem. Mater.*, 2020, **32**, 7932–7940.
95 G. Rogl, A. Grytsiv, P. Rogl, N. Peranio, E. Bauer, M. Zehetbauer and O. Eibl, *Acta Mater.*, 2014, **63**, 30–43.
96 R. S. Feigelson, *Preparation and Evaluation of Phosphide Skutterudites*, Geballe Laboratory for Advanced Materials, 2001.
97 D. J. Singh and W. E. Pickett, *Phys. Rev. B: Condens. Matter Mater. Phys.*, 1994, **50**, 11235–11238.
98 M. Llunell, P. Alemany, S. Alvarez, V. P. Zhukov and A. Vernes, *Phys. Rev. B: Condens. Matter Mater. Phys.*, 1996, **53**, 10605–10609.
99 A. Watcharapasorn, R. C. DeMattei, R. S. Feigelson, T. Caillat, A. Borshchevsky, G. J. Snyder and J. P. Fleurial, *J. Appl. Phys.*, 1999, **86**, 6213–6217.
100 G. Murtaza, N. Yousaf, M. Yaseen, A. Laref and S. Azam, *Mater. Res. Express*, 2018, **5**, 016304.
101 F. H. Sun, S. F. Ma, W. Y. Zhao, C. C. Li, X. H. Sang, P. Wei and Q. J. Zhang, *Rep. Prog. Phys.*, 2021, **84**, 096501.
102 S. Hébert, R. Daou, A. Maignan, S. Das, A. Banerjee, Y. Klein, C. Bourgès, N. Tsujii and T. Mori, *Sci. Technol. Adv. Mater.*, 2021, **22**, 583–596.
103 S. S. Stoyko, P. E. R. Blanchard, K. K. Ramachandran and A. Mar, *J. Solid State Chem.*, 2019, **269**, 100–106.
104 A. Balvanz, S. Baranets, M. O. Ogunbunmi and S. Bobev, *Inorg. Chem.*, 2021, **60**, 14426–14435.
105 J. Rauscher, C. Condron, T. Beault, S. Kauzlarich, N. Jensen, P. Klavins, S. MaQuilon, Z. Fisk and M. Olmstead, *Acta*

Crystallogr., Sect. C: Cryst. Struct. Commun., 2009, **65**, i69–i73.
106 T. Graf, C. Felser and S. S. P. Parkin, *Prog. Solid State Chem.*, 2011, **39**, 1–50.
107 B. W. Montag, M. A. Reichenberger, K. R. Arpin, M. Sunder, K. A. Nelson, P. B. Ugorowski and D. S. McGregor, *J. Cryst. Growth*, 2015, **412**, 103–108.
108 Z. Liu, J. Mao, J. Sui and Z. Ren, *Energy Environ. Sci.*, 2018, **11**, 23.
109 Y. Zheng, C. Liu, L. Miao, C. Li, R. Huang, J. Gao, X. Wang, J. Chen, Y. Zhou and E. Nishibori, *Nano Energy*, 2019, **59**, 311–320.
110 P. Ying, L. Wilkens, H. Reith, N. P. Rodriguez, X. Hong, Q. Lu, C. Hess, K. Nielsch and R. He, *Energy Environ. Sci.*, 2022, **15**, 2557–2566.
111 A. Yamakage, Y. Yamakawa, Y. Tanaka and Y. Okamoto, *J. Phys. Soc. Jpn.*, 2016, **85**, 013708.
112 Y. Okamoto, T. Inohara, A. Yamakage, Y. Yamakawa and K. Takenaka, *J. Phys. Soc. Jpn.*, 2016, **85**, 123701.
113 N. Xu, Y. T. Qian, Q. S. Wu, G. Autes, C. E. Matt, B. Q. Lv, M. Y. Yao, V. N. Strocov, E. Pomjakushina, K. Conder, N. C. Plumb, M. Radovic, O. V. Yazyev, T. Qian, H. Ding, J. Mesot and M. Shi, *Phys. Rev. B*, 2018, **97**, 161111R.
114 A. Mewis, *Z. Naturforsch., B: J. Chem. Sci.*, 1979, **34**, 14–17.
115 U.-G. Jong, C. Ryu, C.-J. Kang and C.-J. Yu, *Appl. Phys. Lett.*, 2023, **122**, 133905.
116 A. Mewis, *Z. Naturforsch., B: J. Chem. Sci.*, 1978, **33**, 983–986.
117 A. Mewis, *Z. Naturforsch., B: J. Chem. Sci.*, 1979, **34**, 1373–1376.
118 J. Willis, I. Bravić, R. R. Schnepf, K. N. Heinselman, B. Monserrat, T. Unold, A. Zakutayev, D. O. Scanlon and A. Crovetto, *Chem. Sci.*, 2022, **13**, 5872–5883.
119 W. Żdanowicz and A. Wojakowski, *Phys. Status Solidi B*, 1965, **8**, 569–575.
120 H. Wang, X. Luo, W. Chen, N. Wang, B. Lei, F. Meng, C. Shang, L. Ma, T. Wu, X. Dai, Z. Wang and X. Chen, *Sci. Bull.*, 2018, **63**, 411–418.
121 J. Yu, C. Fu, Y. Liu, K. Xia, U. Aydemir, T. C. Chasapis, G. J. Snyder, X. Zhao and T. Zhu, *Adv. Energy Mater.*, 2018, **8**, 1701313.
122 W. Ren, H. Zhu, J. Mao, L. You, S. Song, T. Tong, J. Bao, J. Luo, Z. Wang and Z. Ren, *Adv. Electron. Mater.*, 2019, **5**, 1900166.
123 H. B. Kang, B. Poudel, W. Li, H. Lee, U. Saparamadu, A. Nozariasbmarz, M. G. Kang, A. Gupta, J. J. Heremans and S. Priya, *Mater. Today*, 2020, **36**, 63–72.
124 U. G. Jong, C. H. Ri, C. J. Pak, C. H. Kim, S. Cottenier and C. J. Yu, *New J. Chem.*, 2021, **45**, 21569–21576.
125 K. Pal, J. G. He and C. Wolverton, *Chem. Mater.*, 2018, **30**, 7760–7768.
126 M. Miyata, *J. Appl. Phys.*, 2021, **130**, 035104.
127 H. Wang, Y. Pei, A. D. LaLonde and G. J. Snyder, *Proc. Natl. Acad. Sci. U.S.A.*, 2012, **109**, 9705–9709.
128 H. Wang, R. Gurunathan, C. Fu, R. Cui, T. Zhu and G. J. Snyder, *Mater. Adv.*, 2022, **3**, 734–755.
129 P. Graziosi, C. Kumarasinghe and N. Neophytou, *ACS Appl. Energy Mater.*, 2020, **3**, 5913–5926.
130 D. Yang, X. Su, J. Li, H. Bai, S. Wang, Z. Li, H. Tang, K. Tang, T. Luo, Y. Yan, J. Wu, J. Yang, Q. Zhang, C. Uher, M. G. Kanatzidis and X. Tang, *Adv. Mater.*, 2020, **32**, 2003730.